© 2020. Published by The Company of Biologists Ltd | Development (2020) 147, dev183764. doi:10.1242/dev.183764

RESEARCH ARTICLE

CXXC finger protein 1-mediated histone H3 lysine-4 trimethylation is essential for proper meiotic crossover formation in mice

Yu Jiang[1,*], Hui-Ying Zhang[1,*], Zhen Lin[2,*], Ye-Zhang Zhu[1], Chao Yu[1], Qian-Qian Sha[1], Ming-Han Tong[2,‡], Li Shen[1,‡] and Heng-Yu Fan[1,3,‡]

ABSTRACT

The most significant feature of meiosis is the recombination process during prophase I. CXXC finger protein 1 (CXXC1) binds to CpG islands and mediates the deposition of H3K4me3 by the SETD1 complex. CXXC1 is also predicted to recruit H3K4me3-marked regions to the chromosome axis for the generation of double-strand breaks (DSBs) in the prophase of meiosis. Therefore, we deleted *Cxxc1* before the onset of meiosis with *Stra8-Cre*. The conditional knockout mice were completely sterile with spermatogenesis arrested at MII. Knockout of *Cxxc1* led to a decrease in the H3K4me3 level from the pachytene to the MII stage and caused transcriptional disorder. Many spermatogenesis pathway genes were expressed early leading to abnormal acrosome formation in arrested MII cells. In meiotic prophase, deletion of *Cxxc1* caused delayed DSB repair and improper crossover formation in cells at the pachytene stage, and more than half of the diplotene cells exhibited precocious homologous chromosome segregation in both male and female meiosis. *Cxxc1* deletion also led to a significant decrease of H3K4me3 enrichment at DMC1-binding sites, which might compromise DSB generation. Taken together, our results show that CXXC1 is essential for proper meiotic crossover formation in mice and suggest that CXXC1-mediated H3K4me3 plays an essential role in meiotic prophase of spermatogenesis and oogenesis.

KEY WORDS: Meiosis, Spermatogenesis, Oocyte, Histone methylation, Chromosome, Fertility, CFP1

INTRODUCTION

During meiosis, a diploid cell produces haploid gametes with two consecutive rounds of division. Unique chromosomal events occur during the prophase of meiosis I, including genome-wide homologous recombination, initiated by programmed formation of double-strand breaks (DSBs). Successful homologous recombination is essential for proper chromosome segregation and fertility (Hunter, 2015).

[1]MOE Key Laboratory for Biosystems Homeostasis & Protection and Innovation Center for Cell Signaling Network, Life Sciences Institute, Zhejiang University, Hangzhou 310058, China. [2]State Key Laboratory of Molecular Biology, Shanghai Key Laboratory of Molecular Andrology, CAS Center for Excellence in Molecular Cell Science, Shanghai Institute of Biochemistry and Cell Biology, Chinese Academy of Sciences, University of Chinese Academy of Sciences, Shanghai 200031, China. [3]Key Laboratory of Reproductive Dysfunction Management of Zhejiang Province, Assisted Reproduction Unit, Department of Obstetrics and Gynecology, Sir Run Run Shaw Hospital, School of Medicine, Zhejiang University, Hangzhou 310016, China.
*These authors contributed equally to this work

‡Authors for correspondence (hyfan@zju.edu.cn; li_shen@zju.edu.cn; minghan@sibcb.ac.cn)

M.-H.T., 0000-0002-1967-5927; L.S., 0000-0002-5696-2191; H.-Y.F., 0000-0003-4544-4724

Received 9 August 2019; Accepted 14 February 2020

Among several regulated factors, histone modifications play an important role in initiating and regulating chromosomal events during meiosis (Hinch et al., 2019). Evolutionarily conserved from yeast to human, trimethylated histone H3 at lysine-4 (H3K4me3) is a prominent mark of active meiotic recombination initiation sites (Borde et al., 2009). In *Saccharomyces cerevisiae*, the H3K4 trimethylase SET1 is required for DSB formation, which initiates homologous recombination in meiotic prophase (Sollier et al., 2004). In mammals, meiotic recombination occurs at 1- to 2-kb genomic regions termed hotspots (de Massy, 2013a; Paigen and Petkov, 2010), the positions and activities of which are determined by another DNA-binding histone methyltransferase, PRDM9 (Baudat et al., 2010; Berg et al., 2010; Diagouraga et al., 2018; Parvanov et al., 2010). Hypothetically, PRDM9 forms complexes with additional proteins, including CXXC finger protein 1 (CXXC1; also known as CFP1), thereby bringing hotspot DNA to the chromosomal axis, and providing the appropriate environment to allow hotspots to proceed into the next phase of recombination (Parvanov et al., 2017; Tian et al., 2018). However, *in vivo* evidence is lacking to support the role of CXXC1 in homologous chromosomal recombination.

CXXC1 is a DNA-binding component of the SETD1 methyltransferase complex. CXXC1 targets SETD1A/B to most CpG islands (CpGI) and mediates the generation of H3K4me3 (Thomson et al., 2010). Deficiency of *Cxxc1* in mice leads to peri-implantation lethality (Carlone and Skalnik, 2001). To study the *in vivo* functions of CXXC1, several groups have independently generated *Cxxc1*$^{flox/flox}$ mouse strains for CRE recombinase-mediated conditional knockout (Cao et al., 2016; Chun et al., 2014; Tian et al., 2018). Deletion of *Cxxc1* in oocytes blocks the accumulation of H3K4me3 on chromatin during oogenesis and significantly impairs meiotic maturation and the subsequent maternal-to-zygotic transition (MZT) (Yu et al., 2017). Moreover, CXXC1 and H3K4me3 play transcription-independent roles in mediating meiotic and mitotic cell cycle progression, including G2-M phase transition, spindle assembly, and chromosome condensation and alignment, in oocytes and early embryos (Sha et al., 2018). These data all suggest an indispensable role of *Cxxc1* in germ cell development and meiosis. In these studies, however, promoters of mouse *Gdf9* and *Zp3* genes were used to drive CRE expression and *Cxxc1* knockout in female germ cells (Sha et al., 2018; Yu et al., 2017). *Cxxc1* deletion was only accomplished by postnatal day(P) 3 and 5, respectively, when oocytes have developed to the diplotene stage of meiotic prophase and are enclosed in primordial and primary follicles. Therefore, it remains unclear whether CXXC1-mediated H3K4 trimethylation is also required for the earliest stages of meiosis in both male and female germ cells.

To answer this question, we selectively deleted *Cxxc1* in pre-meiotic germ cells using a recently generated *Stra8-Cre* knock-in

Development (2020) 147, dev183764. doi:10.1242/dev.183764

mouse strain (*Cxxc1*$^{fl/-}$*;Stra8-Cre*) (Lin et al., 2017). In contrast to previously used *Stra8-Cre* transgenic mice, in which the transgene is only expressed in male germ cells (Sadate-Ngatchou et al., 2008), CRE recombinase is expressed in both sexes of the *Stra8-Cre* knock-in mice. Another group has reported that conditional knockout of *Cxxc1* using the transgenic *Stra8-Cre* did not affect spermatogenesis and male fertility (Tian et al., 2018). In contrast, our results indicate that *Cxxc1* deletion in pre-meiotic germ cells using the *Stra8-Cre* knock-in mice causes a decrease of H3K4me3 levels in spermatocytes after the zygotene stage, and impairs DSB repair and crossover formation in meiotic prophase. *Cxxc1*-deleted spermatocytes failed to complete meiosis and were arrested at the secondary spermatocyte stage. RNA sequencing (RNA-seq) and H3K4me3 chromatin immunoprecipitation with sequencing (ChIP-seq) results further indicate that CXXC1 is required for H3K4me3 accumulation at the gene promoters of male germ cells and plays a key role in regulating the programmed gene expression that is essential for spermatogenesis.

RESULTS

CXXC1 is required for H3K4me3 maintenance in spermatocytes

To explore the role of CXXC1 in regulating H3K4me3 during spermatogenesis, we first examined the expression pattern of CXXC1 in mouse testes. A published single-cell RNA-seq dataset (Chen et al., 2018) (Fig. S1A) indicates that *Cxxc1* remains highly expressed from spermatogonia to meiotic cells. We verified the high expression of CXXC1 in undifferentiated spermatogonia by co-staining with LIN28A (Fig. S1B). Immunohistochemistry (IHC) results showed that CXXC1 protein is mainly expressed in the nucleus of spermatocytes of all stages and round spermatids, but was undetectable in dividing spermatocytes and elongated spermatids (Fig. 1A). Western blotting results further confirmed the expression of CXXC1 in spermatocytes isolated by flow cytometry (Fig. 1B). The purity of isolated meiotic prophase I cells was verified with SYCP3-γH2AX staining (Fig. S1C,D) and the purity of isolated secondary spermatocytes was verified with X-Y chromosome fluorescent *in situ* hybridization (FISH) staining (Fig. S1E); 94% of diploid cells (n=109) isolated by fluorescence-activated cell sorting (FACS) were secondary spermatocytes with either X or Y chromosome labeling. To determine the role of *Cxxc1* during mammalian meiosis, we used a conditional knockout (cKO) approach in which a *Cxxc1* floxed line (*Cxxc1*$^{fl/fl}$, in which exons 4 and 5 of the *Cxxc1* allele are flanked by *loxP* sites) (Cao et al., 2016) was crossed with *Stra8-Cre* knock-in mice expressing CRE from the A1 spermatogonia stage onward (Lin et al., 2017). We verified the efficiency of Cre-mediated recombination by separately genotyping somatic cells and Cre-mediated recombined germ cells (Fig. S1F). Western blot results also verified that CXXC1 was undetectable in spermatocytes purified from *Cxxc1*$^{fl/-}$*;Stra8-Cre* mice (Fig. 1B). The knockout efficiency was also verified by western blotting with another CXXC1 N-terminal antibody (Fig. S1G).

As the SETD1-CXXC1 complex is considered the main histone H3K4me3 methyltransferase in mammalian cells, we next analyzed the effect of *Cxxc1* knockout on H3K4 methylation in mouse spermatocytes. In wild-type (WT) spermatocytes, H3K4me1, H3K4me2 and H3K4me3 all exhibited strong signals at the leptotene and zygotene stages and weaker (but still noteworthy) signals in the pachytene and diplotene stages as well as the secondary spermatocyte stage (Fig. 1B). Notably, H3K4me3 signals were significantly reduced at and after the pachytene stage in *Cxxc1*$^{fl/-}$*;Stra8-Cre* mice, whereas H3K4me1 and H3K4me2 levels were unaffected by *Cxxc1* deletion. Taken together, these observations indicate that CXXC1 is required for maintaining the H3K4me3 level in spermatocytes. Immunofluorescence (IF) staining results on meiotic spreads also showed a significant decrease of H3K4me3 levels in *Cxxc1* null spermatocytes at the pachytene and diplotene stages (Fig. 1C,D). We also performed IF staining on testicular sections and got the same results (Fig. S1H,I). Because CRE recombinase is also expressed in female pre-meiotic germ cells in the *Stra8-Cre* knock-in mice, we also examined H3K4me3 levels in oocytes at the meiotic prophase I stage (P17.5). Similar to the results in spermatocytes, H3K4me3 levels transiently decreased at the pachytene stage and then re-accumulated at the diplotene stage in WT oocytes; in contrast, the re-accumulation of H3K4me3 failed in *Cxxc1*-deleted oocytes (Fig. 1E,F). Collectively, these results indicate that CXXC1 is involved in the regulation of H3K4 trimethylation during meiotic prophase I, and is potentially important for meiotic cell cycle progression.

CXXC1 is essential for murine spermatogenesis

Although the *Cxxc1*$^{fl/-}$*;Stra8-Cre* males copulated normally, they were completely sterile (Fig. 2A). Testes from pubertal and adult *Cxxc1*$^{fl/-}$*;Stra8-Cre* mice were significantly smaller than those of the littermate controls (Fig. 2B,C). Immunofluorescence staining results of the germ cell marker mouse VASA homolog (MVH; also known as DDX4) and the DSB marker phosphorylated histone H2AX (γH2AX) indicated that the testicular seminiferous tubules of adult *Cxxc1*$^{fl/-}$*; Stra8-Cre* mice contained multiple layers of germ cells, which had entered meiosis and initiated the process of programmed DSB formation (Fig. 2D). Histological examination of 6-week-old germ cell mutant testes showed that the seminiferous tubules were devoid of elongating and elongated spermatids and contained exclusively multinucleated giant cells formed by apoptotic spermatids (Fig. 2E). Consistent with this, no sperm were found in the epididymis of adult *Cxxc1*$^{fl/-}$*;Stra8-Cre* mice (Fig. 2F). These results suggest that CXXC1 plays an essential role in spermatogenesis, and its loss leads to abnormalities in early spermatid development.

Cxxc1-deleted spermatocytes are finally arrested at the secondary spermatocyte stage

When different groups of spermatogenic cells were sorted by FACS, there were no haploid round spermatids in *Cxxc1*$^{fl/-}$*;Stra8-Cre* mice. Testes of *Cxxc1*$^{fl/-}$*;Stra8-Cre* mice contained more diploid spermatocytes than did control mice (Fig. 3A), indicating that *Cxxc1*-deleted spermatocytes were arrested at the secondary spermatocyte stage. We also found abnormal metaphase cells that contained lagging chromosomes on Hematoxylin and Eosin (H&E)-stained sections of *Cxxc1*$^{fl/-}$*;Stra8-Cre* mice (Fig. 3B). To examine the karyotypes more closely, we made spermatocyte chromosome spreads (Fig. 3C). The spermatocytes in *Cxxc1*$^{fl/-}$*; Stra8-Cre* mice exhibited an increase in premature separated univalent chromosomes during meiosis I (chromosome number >20) compared with those in control mice, indicating that meiotic metaphase I is also disordered upon *Cxxc1* mutation (Fig. 3D).

Additionally, we performed IF staining on testis sections with FITC-conjugated peanut agglutinin (PNA), which marks the outer acrosomal membrane of spermatids. Surprisingly, PNA signals were still detected in *Cxxc1*$^{fl/-}$*;Stra8-Cre* tubules despite the lack of spermatids in them (Fig. 3E). We speculated that the PNA signals were on the arrested secondary spermatocytes. To confirm this, we performed FITC-PNA immunocytofluorescence staining on FACS-sorted haploid spermatids from control mice and the diploid MII spermatocytes from *Cxxc1*$^{fl/-}$*;Stra8-Cre* mice. The results

Development (2020) 147, dev183764. doi:10.1242/dev.183764

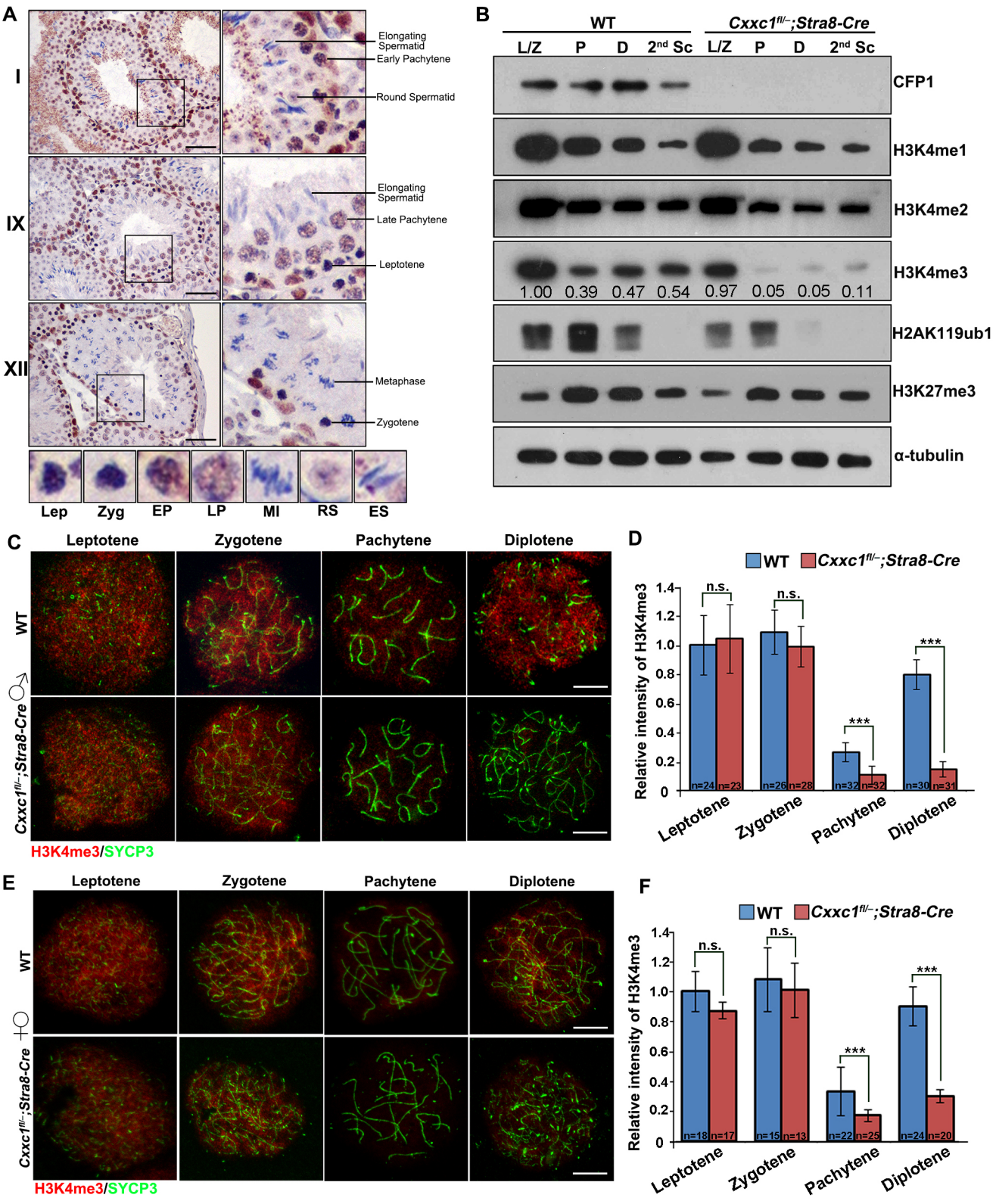

Fig. 1. See next page for legend.

showed that the MII-arrested *Cxxc1*-deleted spermatocytes were indeed positive for PNA signals (Fig. 3F). Moreover, at all three acrosomal differentiating phases (Golgi phase, cap phase and acrosome phase), the *Cxxc1* null spermatocytes exhibited abnormal acrosome structures (Fig. 3E). Collectively, these results indicate that *Cxxc1* null spermatocytes are partially arrested at MI stage. However, there were still a significant number of spermatocytes that could escape from the spindle checkpoint and these were able to develop into the secondary spermatocytes but failed to finish meiosis and initiated false acrosome biogenesis ahead of time.

Development (2020) 147, dev183764. doi:10.1242/dev.183764

Fig. 1. CXXC1 is indispensable for H3K4me3 maintenance during spermatogenesis. (A) Immunohistochemistry staining of CXXC1 in testes of 12-week-old WT mice. Higher magnifications of the boxed areas are shown to the right. Scale bars: 50 µm. EP, early pachytene; ES, elongating spermatids; Lep, leptotene; LP, late pachytene; MI, meiosis I; RS, round spermatids; Zyg, zygotene. (B) Western blot of CXXC1 (CFP1) and epigenetically modified histones in spermatogenic cells isolated from adult WT and *Cxxc1*$^{fl/-}$*;Stra8-Cre* mice. H3K4me3 signal intensity values are labeled (relative to L/Z). D, diplotene; L/Z, leptotene/zygotene; P, pachytene; 2nd Sc, second spermatocytes. (C) Immunofluorescence staining of H3K4me3 in spermatocyte spreads made from adult WT and *Cxxc1*$^{fl/-}$*;Stra8-Cre* mice. Scale bars: 10 µm. (D) Quantification of the H3K4me3 signals shown in C. Numbers of analyzed spermatocytes are indicated (*n*). Error bars, s.e.m. ***P<0.001 (two-tailed Student's *t*-tests). n.s., non-significant.
(E) Immunofluorescence staining of H3K4me3 in oocyte spreads made from WT and *Cxxc1*$^{fl/-}$*;Stra8-Cre* female mice at P17.5. Scale bars: 10 µm.
(F) Quantification of the H3K4me3 signals shown in E. Numbers of analyzed oocytes are indicated (*n*). Error bars, s.e.m. ***P<0.001 (two-tailed Student's *t*-tests). n.s., non-significant.

Meiotic DSB repair and potential crossover loci are impaired in *Cxxc1* null spermatocytes

To investigate further whether the DSB repair process and chromosomal synapsis are impaired after *Cxxc1* knockout, we used co-immunofluorescence staining for phosphorylated H2AX (γH2AX), which marks unrepaired DNA lesions and the sex body in pachynema, and synaptonemal complex protein 3 (SYCP3), which marks the synaptonemal complex, to test for the processing of recombination repair. The pattern of γH2AX signals was largely unchanged in *Cxxc1* knockout compared with the WT control spermatocytes, with γH2AX signal observed throughout the nucleus in leptonema and zygonema, when DSBs occur, and then restricted to the sex body in pachynema and diplonema, when the autosomal breaks are repaired (Fig. 4A). However, we detected unrepaired DSBs with γH2AX signals partially retained on autosomes in 62.7% of *Cxxc1* null pachynema (Fig. 4B). The DSB number was further determined by immunostaining of DMC1 and RAD51, two markers reflecting different stages of DSB processing (Barlow et al., 1997; Pittman et al., 1998). *Cxxc1* knockout did not change the numbers of DMC1 and RAD51 foci in early zygotene and late zygotene spermatocytes. However, whereas the numbers of DMC1 and RAD51 foci largely decreased at the early pachytene stage in WT spermatocytes, more foci persisted in *Cxxc1* null spermatocytes (Fig. 4C,D).

We also measured primary spermatocyte proportions based on γH2AX and SYCP3 double staining and did not detect a difference in the proportions of spermatocytes at any stage of meiotic prophase I (Fig. 5A). Nevertheless, we observed precociously separated homologous chromosomes in 56.1% of *Cxxc1* null diplonema, versus 12.8% in control (Fig. 5B). Co-immunostaining of SYCP1 and SYCP3 at the diplotene stage confirmed the dissociation of synapsis in these precociously separated chromosomes (Fig. 5C). This result suggested defects of crossover formation or resolution in *Cxxc1* null spermatocytes. Therefore, we examined the number and location of potential crossover sites in pachynema using MLH1 as a marker. We observed a significant increase in potential crossover numbers in the *Cxxc1* null pachynema compared with the controls (Fig. 5D). With further analysis of MLH1 distribution, we found that in *Cxxc1* null pachynema, there were more chromosomes with two MLH1 sites, but at least one MLH1 site formed in almost all chromosomes (Fig. 5E,F). We also found more MLH1 sites on *Cxxc1* null cell chromosomes located near to the centromere, which are more likely to cause chromosome segregation (Fig. 5E,G) (Mézard et al., 2015; Sherman et al., 1994; Vincenten et al., 2015). Above all, the whole spermatogenesis processes in WT and *Cxxc1* null mice were briefly concluded (Fig. 5H).

RNA-seq analyses of spermatocytes derived from WT and *Cxxc1* cKO mice

To understand further the role of CXXC1 in spermatogenesis at the molecular level, we performed RNA-seq analyses in WT and *Cxxc1* null spermatocytes at pachytene, diplotene and MII stages. Gene expression levels were assessed as fragments per kilobase of transcript per million mapped reads (FPKM). All samples were analyzed in duplicate, and the replicates showed high correlations (Table S1, Fig. S2A). The numbers of upregulated genes in *Cxxc1* null spermatocytes were similar at the three stages (649 for pachytene, 845 for diplotene and 829 for MII; Fig. 6A, Fig. S2B,C). As shown in Fig. 6B, 71% of upregulated genes at the pachytene stage (463 out of 649 genes) were also upregulated at the diplotene stages. Gene ontology analysis revealed that these genes were significantly enriched in terms relating to the spermatogenesis pathway, including positive regulation of acrosome reaction (Fig. S2D,E). We then examined the expression of upregulated genes within the spermatogenesis pathway across different stages in WT spermatocytes and found that they were upregulated at the MII stage (Fig. 6C, left), suggesting an earlier expression of these genes in *Cxxc1* null spermatocytes. Indeed, the expression level of these genes in *Cxxc1* null pachytene/diplotene spermatocytes was comparable to that in WT MII-stage cells (Fig. 6C, right). This observation is similar to the early formation of the acrosome in *Cxxc1* null spermatocytes. Furthermore, we analyzed the expression level of acrosome-reaction genes at different stages in WT and *Cxxc1* null spermatocytes, and the results were consistent with an advanced abnormal acrosome phenotype (Fig. S2F,G). By contrast, the number of downregulated genes in *Cxxc1* null spermatocytes at the MII stage (n=744) was much higher compared with those at pachytene (n=143) or diplotene (n=135) stages (Fig. 6D, Fig. S2B,C). The downregulated genes in *Cxxc1* null spermatocytes at the MII stage were significantly enriched in terms relating to chromatin organization, meiotic cell division, and DNA repair pathways (Fig. 6E), which may partially explain the abnormal homologous separation and cell division arrest observed at the MII stage. Note that we verified the knockout efficiency at *Cxxc1* exons 4 and 5 (Fig. S2H). No reads of these two exons were detected, implying that the knockout strategy worked as expected.

H3K4me3 ChIP-seq analyses of leptotene/zygotene and pachytene spermatocytes derived from WT and *Cxxc1* cKO mice

In WT spermatocytes, the global H3K4me3 level dropped at the pachytene stage and recovered at the diplotene stage; however, the H3K4me3 level was even lower and could not be re-established at the diplotene stage in *Cxxc1* null spermatocytes (Fig. 1C,D). To explore further the genome-wide H3K4me3 changes, we performed H3K4me3 ChIP-seq in WT and *Cxxc1* null spermatocytes at the pachytene stage (Table S1). The results showed high correlations between biological replicates (Table S1); therefore, we pooled the biological replicates for further analyses. As shown in Fig. 7A, most genic regions exhibited similar H3K4me3 intensity between WT and *Cxxc1* null spermatocytes, with the exception of promoter and 5′-UTR regions, which showed significantly decreased H3K4me3

Development (2020) 147, dev183764. doi:10.1242/dev.183764

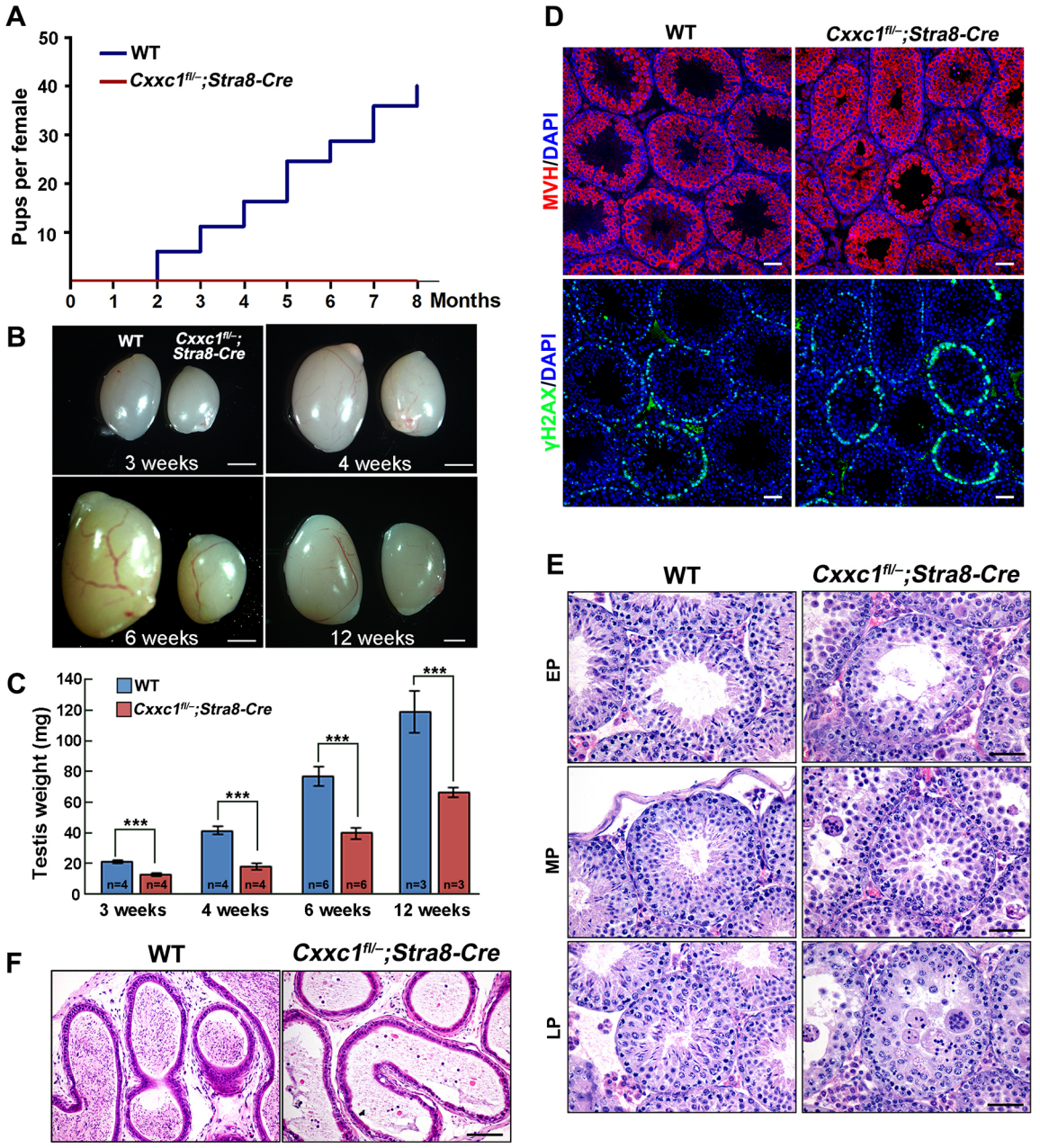

Fig. 2. *Cxxc1* deletion in pre-meiotic germ cells causes spermatogenic defects. (A) Fertility tests showing the average number of pups produced per female at the indicated ages of *Cxxc1*$^{fl/-}$*;Stra8-Cre* and age-matched control mice. *n*=3. (B) Gross morphology of representative testes from *Cxxc1*$^{fl/-}$*;Stra8-Cre* and age-matched control mice. Scale bars: 1 mm. (C) Weights of testes from *Cxxc1*$^{fl/-}$*;Stra8-Cre* and age-matched control mice. Error bars, s.e.m. ***P<0.001 (two-tailed Student's *t*-tests). (D) Immunofluorescence staining of mouse VASA homolog (MVH) and phosphorylated histone H2A.X (γH2AX) in testes of 12-week-old WT and *Cxxc1*$^{fl/-}$*;Stra8-Cre* mice. DNA was counterstained with DAPI. Scale bars: 50 µm. (E,F) H&E staining results showing testis (E) and epididymis (F) histology of 12-week-old control and *Cxxc1*$^{fl/-}$*;Stra8-Cre* mice. EP, early pachytene; LP, late pachytene; MP, middle pachytene. Scale bars: 50 µm.

in *Cxxc1* null spermatocytes. Indeed, H3K4me3 levels were decreased at almost all transcription start sites (TSSs) in *Cxxc1* null spermatocytes compared with WT (Fig. 7C). The general decreases of H3K4me3 at the TSS regions in *Cxxc1* null pachytene spermatocytes prompted us to find out whether H3K4me3 levels were different between WT and *Cxxc1* null spermatocytes at earlier spermatogenesis stages. Therefore, we next performed H3K4me3 ChIP-seq at the leptotene/zygotene stage (Table S2). Correlation of the normalized signal intensity between biological replicates was calculated on genome-wide H3K4me3 depositions (Table S2). Similar to the pachytene stage, H3K4me3 intensity was globally decreased at the promoter and 5′-UTR regions (Fig. 7B, Fig. S3A). In addition, other genic regions, such as exons, introns and 3′-UTRs, also showed decreased H3K4me3 levels although to a lesser extent (Fig. 7B). Because H3K4me3 has been implicated in spermatogenesis by forming DSBs at the leptotene stage, we analyzed changes of H3K4me3 in leptotene/zygotene spermatocytes at known DMC1-binding sites (Tian et al., 2018), a hallmark of meiotic DSBs (Fig. 7D). The result showed significant decreases of H3K4me3 levels at the DMC1-binding sites. We also observed a similar trend of a decrease of H3K4me3 at PRDM9-binding sites (Grey et al.,

Development (2020) 147, dev183764. doi:10.1242/dev.183764

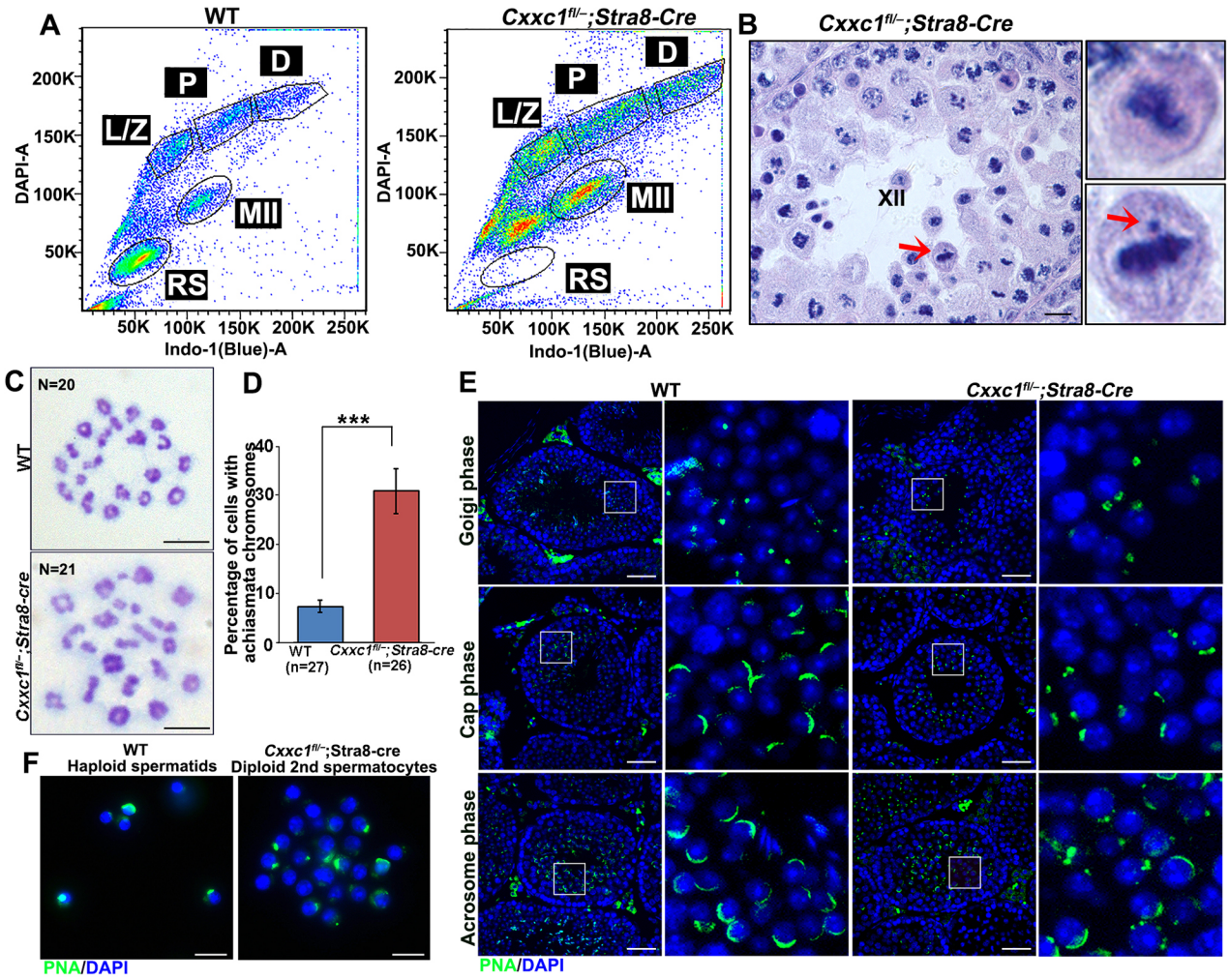

Fig. 3. *Cxxc1* deletion in spermatogenic cells leads to a meiosis II arrest. (A) Gating on individual spermatogenic populations based on Hoechst fluorescence. D, diplotene spermatocytes; L/Z, leptotene/zygotene spermatocytes; MII, meiosis II spermatocytes; P, pachytene spermatocytes; RS, round spermatids. (B) H&E staining of paraffin-embedded testes from *Cxxc1*$^{fl/-}$*;Stra8-Cre* mice. The arrows indicate univalent chromosome lagging in metaphase cells. Scale bar: 10 µm. (C) Representative meiotic metaphase I spreads from control and *Cxxc1*$^{fl/-}$*;Stra8-Cre* mice. N, chromosome number. Scale bars: 10 µm. (D) Percentage of spermatocytes containing achiasmata chromosomes on metaphase I spreads of control and *Cxxc1*$^{fl/-}$*;Stra8-Cre* mice. Numbers of analyzed spermatocytes are indicated (*n*). Error bars, s.e.m. ***P<0.001 (two-tailed Student's *t*-tests). (E) Immunofluorescence staining of FITC-conjugated PNA in sections of control and *Cxxc1*$^{fl/-}$*;Stra8-Cre* mice testes. DNA was counterstained with DAPI. Scale bars: 50 µm. Higher magnifications of the boxed areas are shown to the right and show tubule cross-sections at the Golgi, cap and acrosome phases. Scale bars: 10 µm. (F) Cytofluorescence staining of FITC-conjugated PNA of FACS-isolated round spermatids from control mice and MII spermatocytes from *Cxxc1*$^{fl/-}$*;Stra8-Cre* mice. Scale bars: 50 µm.

2017) at leptotene/zygotene stage (Fig. 7E). Consistent with the formation of the DSBs at the leptotene stage, H3K4me3 enrichment at the DMC1-binding sites almost completely disappeared in both WT and *Cxxc1* null spermatocytes at the pachytene stage (Fig. S3B), indicating a correlation between H3K4me3 and DSB formation.

CXXC1 is required for proper crossover formation during oogenesis

Using an oocyte-specific *Cxxc1* knockout driven by *Gdf9-Cre* (expressed at the primordial follicle stage as early as P3) and *Zp3-Cre* (expressed in awakening primary follicles as early as P5), we have demonstrated that in postnatal oocytes that have passed the meiotic prophase CXXC1 is required for normal meiotic maturation and developmental competence after fertilization. However, the *in vivo* function of CXXC1 at the early phases of oogenesis, particularly in meiotic recombination, were unknown. In the *Stra8-Cre* knock-in mice, Cre recombinase is expressed in both male and female pre-meiotic germ cells. Results of immunofluorescence staining on postnatal ovarian sections confirmed that CXXC1 was deleted and the H3K4me3 level decreased in oocytes of *Cxxc1*$^{fl/-}$*;Stra8-Cre* females (Fig. 8A). The ovaries of *Cxxc1*$^{fl/-}$*;Stra8-Cre* females were consistently smaller than those of control mice at the same age (Fig. 8B,C). At P1, the *Cxxc1*$^{fl/-}$*;Stra8*$^{Cre/+}$ females had fewer oocytes than did the control mice, as determined by quantifying the numbers of MVH-positive oocytes on ovarian serial sections (Fig. 8D,E). Immunostaining on female germ cell spreads at embryonic day (E) 17.5 indicated that *Cxxc1* deletion caused an increase of MLH1 foci (Fig. 8F,G). Double staining of SYCP1 and SYCP3 indicated that synaptonemal complex had formed and dissolved normally in *Cxxc1* null primary oocytes, but precocious separation of homologous chromosomes was detected in nearly half of *Cxxc1* null oocytes (Fig. 8H,I). These results indicated that CXXC1 is required for proper homologous recombination and crossover formation in the meiotic prophase of female germ cells.

Development (2020) 147, dev183764. doi:10.1242/dev.183764

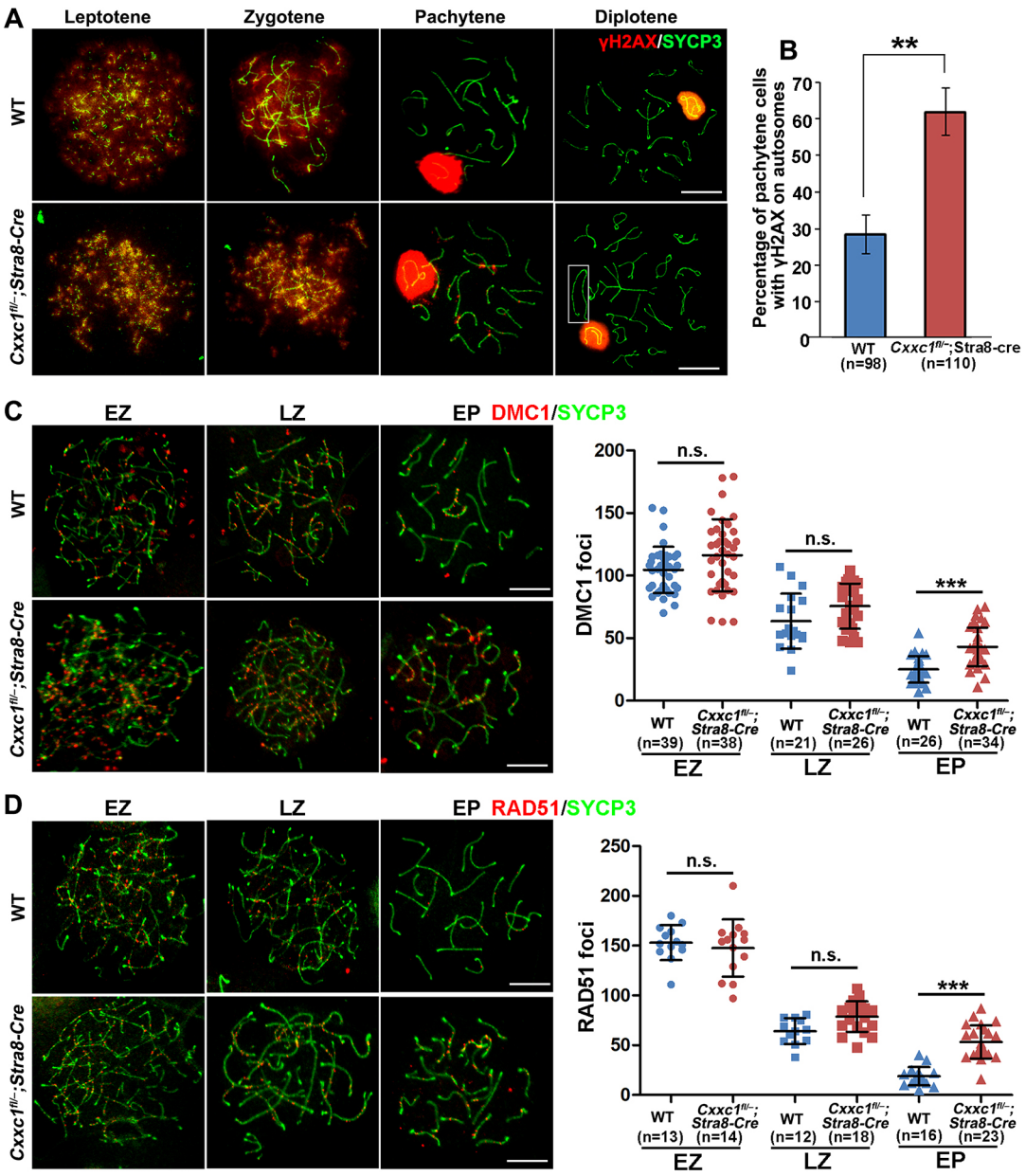

Fig. 4. Impact of *Cxxc1* deletion on DSB formation and repair in spermatogenic cells. (A) Immunofluorescence staining of SYCP3 and γH2AX on spermatocyte spreads made from adult WT and *Cxxc1*$^{fl/-}$*;Stra8-Cre* testes. Boxed area shows precociously separated homologous chromosomes at the diplotene stage. Scale bars: 10 µm. (B) Percentage of pachynema spermatocytes that contained γH2AX foci on their autosomes. Numbers of analyzed spermatocytes are indicated (*n*). Error bars, s.e.m. ***P*<0.01 (two-tailed Student's *t*-tests). (C,D) Immunofluorescence staining of DMC1 (C) and RAD51 (D) on spermatocyte spreads made from WT and *Cxxc1*$^{fl/-}$*;Stra8-Cre* mice. Scale bars: 10 µm. Graphs show quantification of DMC1 (C) and RAD51 (D) foci number per cell at different stages. Numbers of analyzed spermatocytes are indicated (*n*). Error bars, s.e.m. ****P*<0.001 (two-tailed Student's *t*-tests). n.s., non-significant. EP, early pachytene; EZ, early zygotene; LZ, late zygotene.

DISCUSSION

In this study, we investigated the potential role and functional importance of CXXC1 in regulation of H3K4me3 during spermatogenesis. In contrast to recently published reports, our current results show that CXXC1 is required for maintaining normal H3K4me3 levels in mouse spermatocytes, particularly at the pachytene and diplotene stages. In addition, CXXC1 is required for proper DSB repair, crossover formation, and meiotic cell cycle progression during spermatogenesis.

Recently, Tian et al. reported that the knockout of CXXC1 in male germ cells with transgenic *Stra8-Cre* did not impair the meiotic process, and that the knockout mice were fertile (Tian et al., 2018). By contrast, with another knock-in *Stra8-Cre* and using a different knockout strategy, we obtained *Cxxc1* knockout mice that were completely sterile. The H3K4me3 level decreased in *Cxxc1* null spermatocytes, along with improper crossover formation, which caused precocious homologous chromosome separation at the diplotene stage and finally spermatogenesis arrested at MII.

In meiosis, crossover formation is genetically essential for creating new combinations of parental genetic information, and at least one crossover per homologous pair is essential to create a physical connection at the diplotene stage before chromosome

Development (2020) 147, dev183764. doi:10.1242/dev.183764

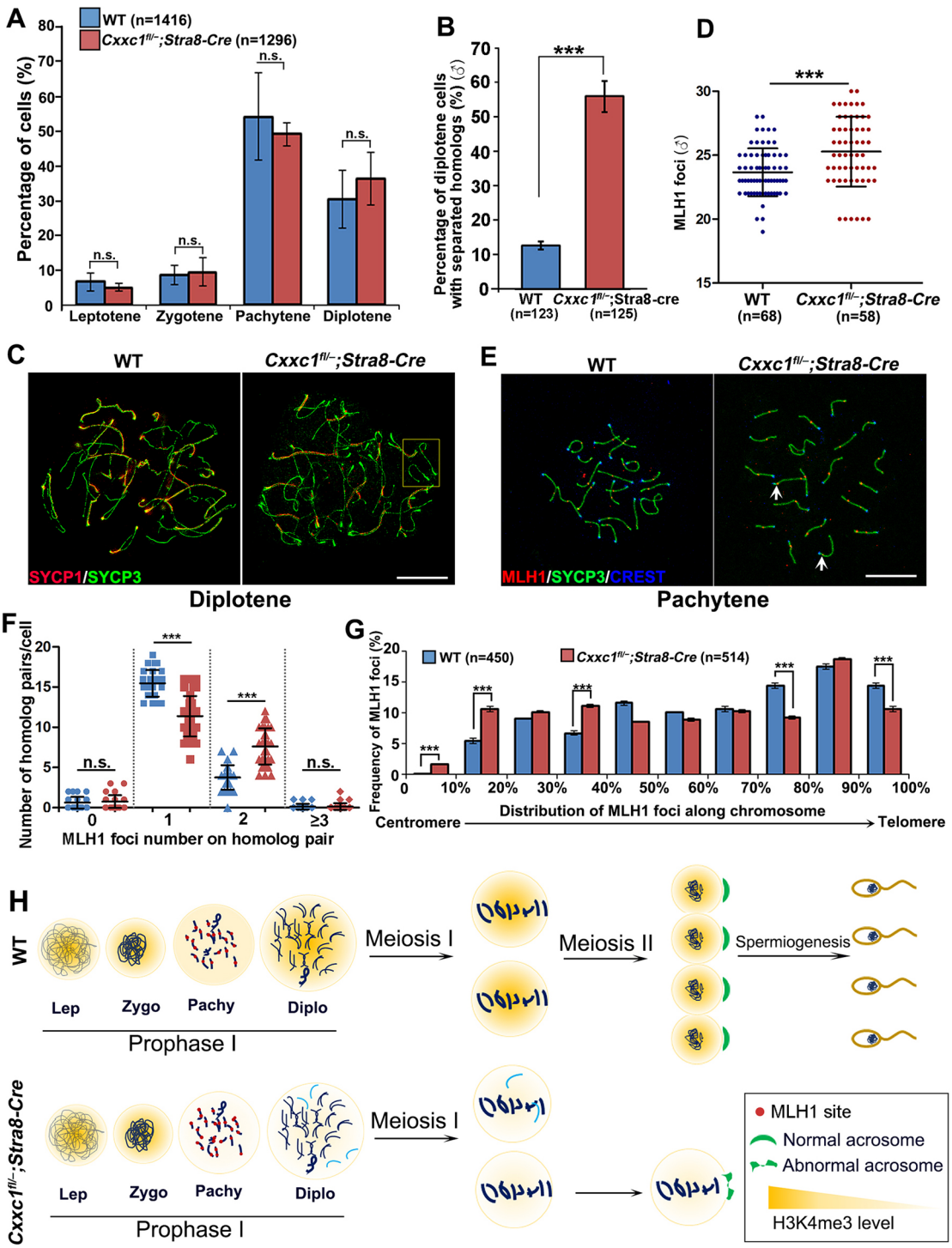

Fig. 5. *Cxxc1* deletion in spermatogenic cells causes improper meiotic crossover formation. (A) Spermatocyte stage proportion in WT and *Cxxc1*$^{fl/-}$;*Stra8-Cre* mice based on SYCP3 and γH2AX immunofluorescence staining of spermatocyte spreads. Numbers of analyzed spermatocytes are indicated (*n*). Error bars, s.e.m. n.s., non-significant (two-tailed Student's t-tests). (B) Percentage of diplonema containing precocious separated homologous chromosomes on spermatocyte spreads of control and *Cxxc1*$^{fl/-}$;*Stra8-Cre* mice. Numbers of analyzed spermatocytes are indicated (*n*). Error bars, s.e.m. ***P<0.001 (two-tailed Student's *t*-tests). (C) Immunofluorescence staining of SYCP1 and SYCP3 on spermatocyte spreads at the diplotene stage. Boxed area shows precociously separated homologous chromosomes at the diplotene stage. Scale bar: 10 µm. (D) Quantification of MLH1 foci from the staining shown in E. Error bars, s.e.m. ***P<0.001 (two-tailed Student's *t*-tests). Numbers of analyzed spermatocytes are indicated (*n*). (E) Immunofluorescence staining of MLH1, CREST (also known as SS18L1) and SYCP3 on spermatocyte spreads at the pachytene stage. Scale bar: 10 µm. White arrows indicate MLH1 loci in *Cxxc1*$^{fl/-}$;*Stra8-Cre* spermatocytes that are close to the centromere. (F) MLH1 foci distribution at different homologous pairs in WT and *Cxxc1*$^{fl/-}$;*Stra8-Cre* spermatocytes. Error bars, s.e.m. ***P<0.001 (two-tailed Student's *t*-tests). n.s., non-significant. (G) Distribution of MLH1 foci along chromosome in WT and *Cxxc1*$^{fl/-}$;*Stra8-Cre* spermatocytes. Numbers of analyzed MLH1 loci are indicated (*n*). Error bars, s.e.m. ***P<0.001 (two-tailed Student's *t*-tests). (H) Schematic showing the function of CXXC1 in meiotic prophase as well as the phenotypes of *Cxxc1*$^{fl/-}$;*Stra8-Cre* mice. The H3K4me3 level is indicated by the depth of yellow shade. *Cxxc1* knockout caused a decrease in H3K4me3 level from the pachytene spermatocyte, along with improper crossover formation (red dots), which caused precocious homologous chromosome separation at the diplotene stage (light blue lines) and finally spermatogenesis arrested at MII with abnormal acrosomal biogenesis.

Development (2020) 147, dev183764. doi:10.1242/dev.183764

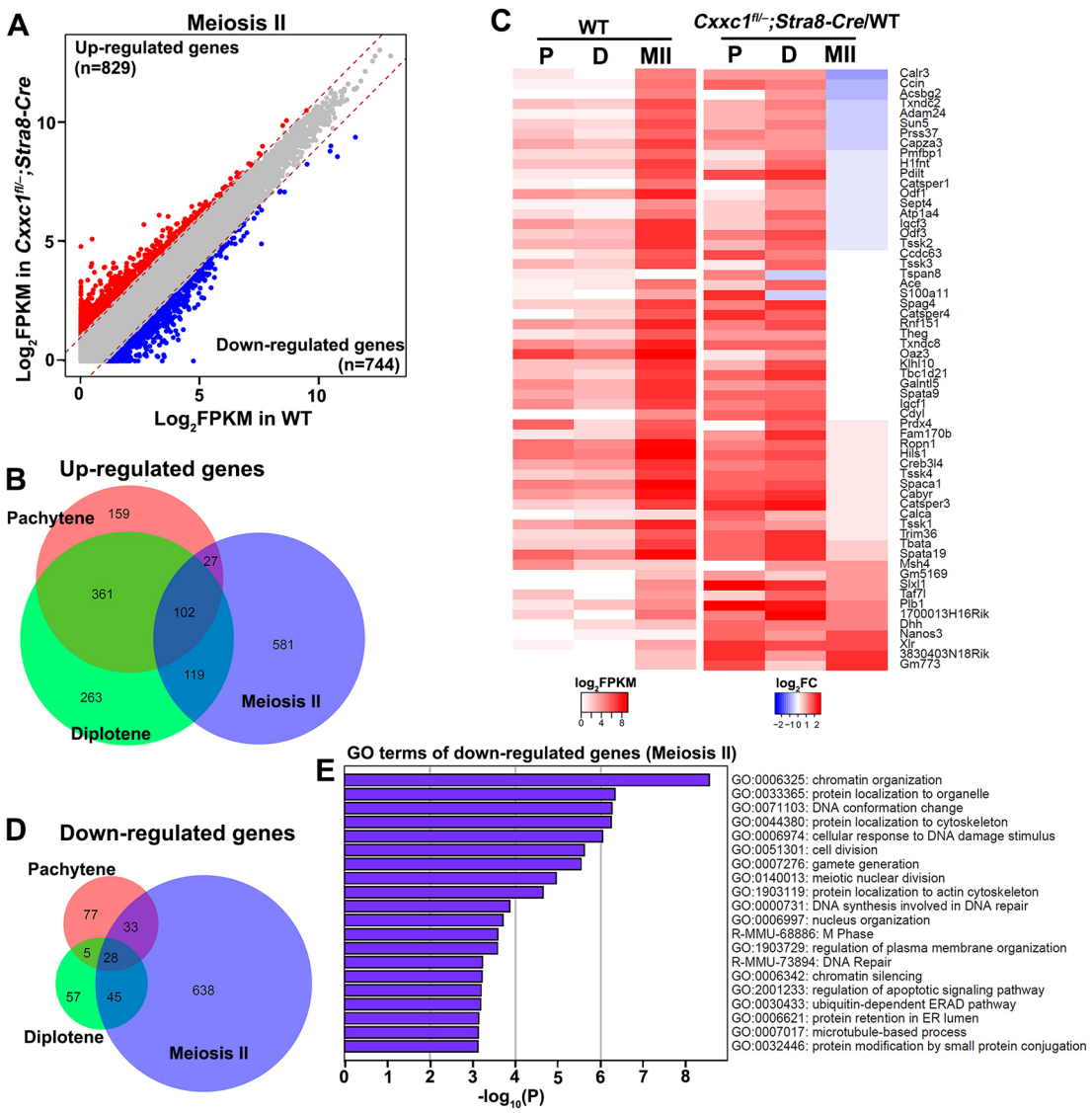

Fig. 6. RNA-seq analyses of pachytene, diplotene and MII spermatocytes derived from WT and *Cxxc1* cKO mice. (A) Scatter plot comparing transcripts between WT and *Cxxc1* cKO spermatocytes at the MII stage. Genes upregulated (FC>2.0) and downregulated (FC<2.0) in *Cxxc1* cKO spermatocytes at the MII stage are colored red and blue, respectively. (B,D) Venn diagrams showing the overlap of genes upregulated (B) and downregulated (D) in *Cxxc1* cKO spermatocytes at different stages. (C) Dynamic profiling of upregulated genes within the spermatogenesis pathway across different stages in WT spermatocytes (left) and clustering analysis of the relative expression levels (right) across the three stages. FC, fold change in *Cxxc1*$^{fl/-}$*;Stra8-Cre* relative to WT. (E) Gene ontology analysis of downregulated genes in *Cxxc1* null spermatocytes at the MII stage.

alignment and accurate segregation in metaphase. Crossovers come from millions of DSBs generated at the leptotene stage. Only a small proportion of DSBs will go through the crossover resolution process; others are repaired during the zygotene to pachytene stages except on the sex chromosomes (Cole et al., 2012). Most recombinations happen at clustered DSB intervals, named hotspots. In mammals, the hotspots are reported to be potentially determined by PRDM9 through its tri-methyltransferase activity on histone H3 lysine-4. But how the histone-modified marked sites are associated with DSB occurrence is still unknown.

In *Saccharomyces cerevisiae*, Spp1, a member of the histone H3K4 methyltransferase Set1 complex, reads H3K4 methylation through its PHD finger domain (Adam et al., 2018), and interacts with the DSB-promoting protein Mer2 on the chromosome axis, thus tethering the H4K4me3-marked chromatin loops to the chromosome axis where DSB formation occurs (de Massy, 2013b; Sommermeyer et al., 2013). In mammals, CXXC1 is the DNA-binding component of the SETD1 methyltransferase complex and also has a PHD finger domain, which is able to recognize H3K4me3 (Mahadevan and Skalnik, 2016; Tian et al., 2018); it has been shown that CXXC1 can interact with the Mer2 ortholog protein IHO1 (CCDC36) by yeast two-hybrid assay (Imai et al., 2017; Stanzione et al., 2016). This suggests that CXXC1 might play a similar function in mammalian meiosis.

Our results showed that knockout of *Cxxc1* in germ cells caused more than half of diplotene spermatocytes to undergo precocious homologous separation, which may result from abnormal crossovers (Fig. 5). The *Cxxc1*$^{fl/-}$*;Stra8-Cre* mice formed more potential crossover sites at the pachytene stage than did WT, but these crossovers were unable to connect as homologous pairs, so we inferred that these crossovers were partially wrong or invalid. For example, *Cxxc1*$^{fl/-}$*;Stra8-Cre* mice formed more potential

Development (2020) 147, dev183764. doi:10.1242/dev.183764

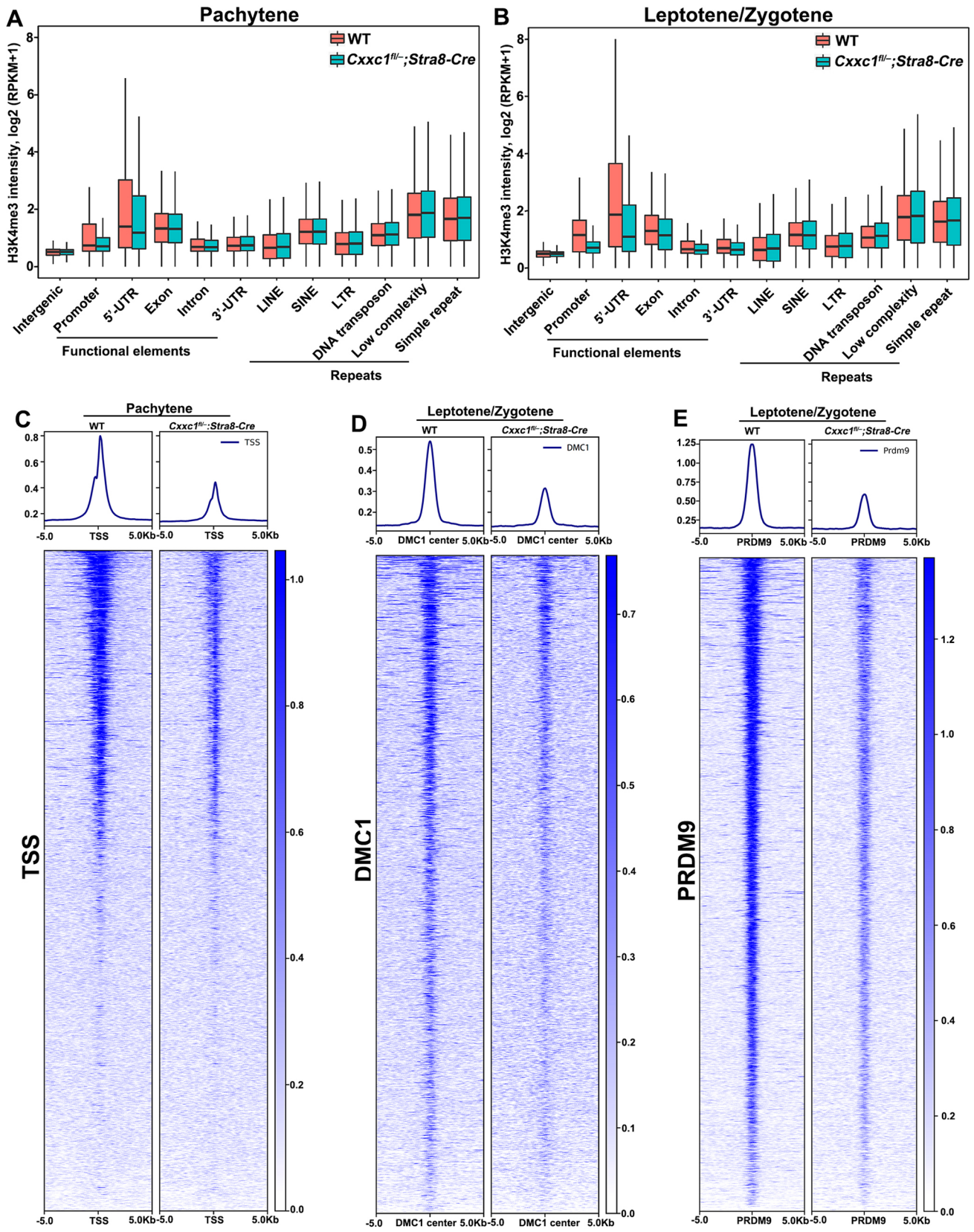

Fig. 7. H3K4me3 ChIP-seq analyses of leptotene/zygotene and pachytene spermatocytes derived from WT and *Cxxc1* cKO mice. (A,B) Box plots showing mean H3K4me3 intensity of WT and *Cxxc1* null spermatocytes at the pachytene (A) and leptotene/zygotene (B) stages in various genic and repetitive sequences. The lower and upper hinges correspond to the first and third quartiles. Thick lines in boxes indicate the medians. The upper whisker extends from the hinge to the largest value no further than 1.5× IQR from the hinge (where IQR is the inter-quartile range, or distance between the first and third quartiles). The lower whisker extends from the hinge to the smallest value at most 1.5× IQR of the hinge. (C-E) Heat map of average H3K4me3 levels in WT and *Cxxc1* null pachytene spermatocytes at the TSS regions (C), at the centers of DMC1-binding sites (D) and at the centers of PRDM9-binding sites (E).

Development (2020) 147, dev183764. doi:10.1242/dev.183764

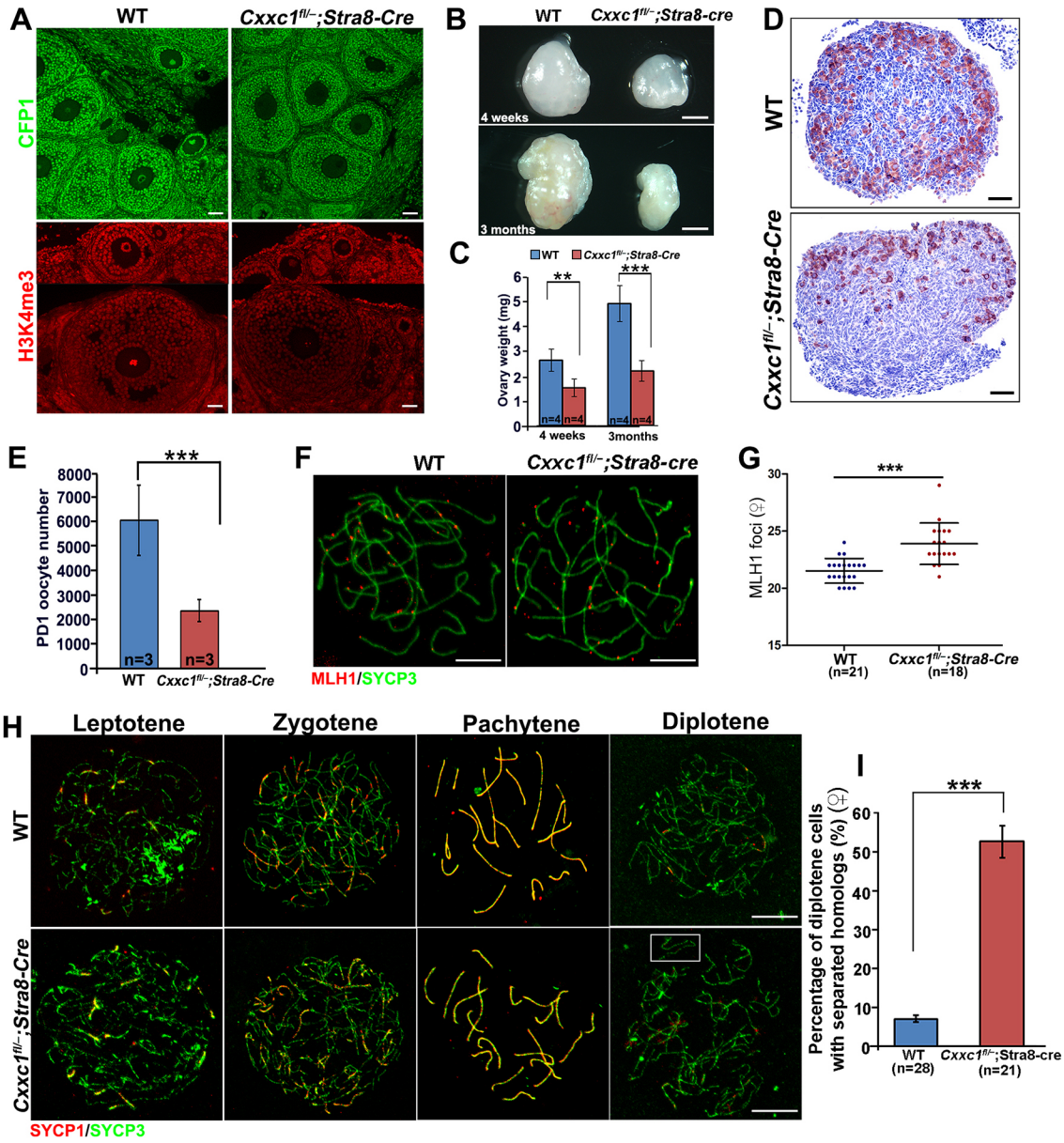

Fig. 8. *Cxxc1* deletion causes improper meiotic crossover formation at the onset of female meiosis. (A) Immunofluorescence staining of CXXC1 (CFP1) and H3K4me3 on ovarian sections prepared from 3-week-old WT and *Cxxc1*$^{fl/-}$*;Stra8-Cre* mice. Scale bars: 50 µm. (B) Ovaries of WT and *Cxxc1*$^{fl/-}$*;Stra8-Cre* mice at the ages of 4 weeks and 3 months. Scale bars: 500 µm. (C) Ovarian weight of WT and *Cxxc1*$^{fl/-}$*;Stra8-Cre* mice at the ages of 4 weeks and 3 months. Error bars, s.e.m. **P<0.01, ***P<0.001 (two-tailed Student's t-tests). (D) MVH immunohistochemistry on ovarian sections prepared from newborn WT and *Cxxc1*$^{fl/-}$*;Stra8-Cre* mice. Scale bars: 50 µm. (E) Numbers of oocytes in ovaries of newborn WT and *Cxxc1*$^{fl/-}$*;Stra8-Cre* mice. Error bars, s.e.m. ***P<0.001 (two-tailed Student's t-tests). Numbers of analyzed ovaries from different mice are indicated (n). (F) Immunofluorescence staining of MLH1 and SYCP3 on oocyte spreads at the pachytene stage. Scale bars: 10 µm. (G) Quantification of the MLH1 foci shown in F. Error bars, s.e.m. ***P<0.001 (two-tailed Student's t-tests). Numbers of analyzed oocytes are indicated (n). (H) Immunofluorescence staining of SYCP1 and SYCP3 on oocyte spreads. Boxed area shows precociously separated homologous chromosomes at the diplotene stage. Scale bars: 10 µm. (I) Percentage of diplonema containing precocious separated homologous chromosomes on oocyte spreads of control and *Cxxc1*$^{fl/-}$*;Stra8*$^{Cre/+}$ mice. Error bars, s.e.m. ***P<0.001 (two-tailed Student's t-tests). Numbers of analyzed oocytes are indicated (n).

crossovers close to the centromere. Since crossovers come from DSBs and the whole process along with highly regulated gene expression, there are several possible reasons for the phenotype of *Cxxc1* deletion.

First, CXXC1 may influence the crossover formation and resolution process. After the DSBs are generated, following strand invasion and double Holliday junction (dHJ) formation and resolution, only a small proportion of DSBs finally become crossovers (Jones, 1984). Other DSBs on autosomes are gradually repaired before mid-pachytene. Errors in crossovers of *Cxxc1*$^{fl/-}$*;Stra8-Cre* mice might come from the dysregulation of the crossover formation and resolution process, along with DSB repair delay (Fig. 4). As Holloway et al. reported, defects in Class II crossover formation also caused MLH1 foci accumulation and delayed DSB repair, which is similar to the *Cxxc1* null spermatocyte phenotype (Holloway et al., 2008).

These improper crossovers might come from improper DSBs generated at the leptotene stage. PRDM9 deposits H3K4me3 at specific sites in the genome, and these sites are recruited to the

Development (2020) 147, dev183764. doi:10.1242/dev.183764

chromosome axis to form DSBs, especially hotspots. We suggest that the lack of CXXC1 might cause loss of this selective mechanism. Thus, other chromatin loops without H3K4me3 modification were randomly tethered to form DSBs resulting in disorder of the canonical hotspots. Crossovers come from DSBs, especially hotspots. So hotspots disorder might cause errors in crossover number and distribution. Consistent with this hypothesis, our ChIP-seq data showed that CXXC1 depletion led to the failure of H3K4me3 enrichment at the known binding sites of DMC1, a marker of canonical DSBs and hotspots.

Moreover, loss of CXXC1 at leptotene/zygotene stage also caused a remarkable decrease of H3K4me3 level at TSSs, suggesting that the gene expression pattern in *Cxxc1* null spermatocytes could be altered as early as the leptotene/zygotene stage, or even earlier. This may also affect the expression of genes related to DSB formation and repair, thereby leading to a delay in DSB repair and a disproportionate crossover distribution. The altered gene expression in pachytene and diplotene stages caused by *Cxxc1* knockout could also affect the distribution of MLH1 and the formation of crossover products after the loading of MLH1, which may explain the failure of chiasma formation despite an increased number of MLH1 foci. Disturbed gene expression at the onset of meiosis may also have contributed to the phenotypes observed at the later stages. Especially at MII, downregulation of genes related to chromatin organization and cell division is likely to cause abnormal MII arrest.

CXXC1 is generally considered to influence H3K4me3 establishment by recruiting the SETD1 complex to DNA-binding sites. However, in this study, at leptotene/zygotene stages we detected no significant change in the expression of components of the SETD1 complex and DNMT1 by RNA-seq of WT and *Cxxc1* null spermatocytes, which is different from its known function that loss of CXXC1 in embryonic stem cells leads to *Dnmt1* transcript levels being significantly elevated (Butler et al., 2009). Moreover, we observed that H2AK119ub1 decreased in *Cxxc1* null spermatocytes (Fig. 1B) and H3K4me3 has been reported to interact with ubH2A in histone-to-protamine exchange during spermiogenesis (Wang et al., 2019). Thus, it is possible that H3K4me3 may have as-yet-unknown interactions with other epigenetic modifications in the spermatogenic process.

MATERIALS AND METHODS

Mice

The conditional mutant alleles for *Cxxc1* (*Cxxc1*$^{flox/flox}$) and the *Stra8-Cre* knock-in mouse strain were generated previously (Cao et al., 2016; Lin et al., 2017). All mice had a C57BL/6J genetic background, and were maintained under specific pathogen-free conditions in a controlled environment of 20-22° C, with a 12/12 h light/dark cycle, 50-70% humidity, and food and water provided *ad libitum*. The experimental protocols involving mice were approved by the Zhejiang University Institutional Animal Care and Research Committee (Approval #ZJU20170014), and mouse care and use were performed in accordance with the relevant guidelines and regulations.

Isolation of spermatogenic cells

We used male mice for preparations of different types of spermatogenic cells as reported (Chen et al., 2018). After removal of the tunica albuginea, testes were incubated in 5 ml PBS with collagenase type I (120 U/ml) at 32°C with gentle agitation for 10 min. The dispersed seminiferous tubules were further digested with 5 ml 0.25% trypsin, plus 0.1 ml DNase I (5 mg/ml) at 32°C for 8 min, and then terminated by adding 0.5 ml fetal bovine serum (FBS). The resulting suspension was passed through a 70 µm cellular filter. After centrifugation at 500 ***g*** for 5 min, cells were resuspended at a concentration of 10^6 cells/ml in DMEM with Hoechst 33342 (5 µg/10^6 cells) and 5 µl DNase I, followed by rotating for 30 min at 32°C at a low speed. Immediately prior to sorting, cells were stained with propidium iodide (PI; 1 µg/10^6 cells) at room temperature. Cell populations were collected based on their fluorescent label with Hoechst 33342/PI staining by FACS using a Flow Cytometer ARIA II (BD Biosciences). Hoechst 33342 was excited using a 355 nm UV laser, and the dye's wide emission spectrum was detected in two distinct channels: the 'Hoechst Blue' (DAPI, 450/50 nm band-pass filter) and the 'Hoechst Red' [Indo-1 (Blue), 530/30 band-pass filter].

Histological and immunofluorescence analyses

Testes were fixed in Bouin's buffer or 4% paraformaldehyde (PFA), embedded in paraffin and sectioned at 5 µm thickness using an ultra-thin semi-automatic microtome (Leica). Sections were deparaffinized, rehydrated, and stained with H&E. For immunofluorescence analysis, sections were boiled in 10 mM sodium citrate buffer (pH 6.0) for 15 min, brought to room temperature, washed and blocked with 10% donkey serum for 60 min, and later incubated with primary antibodies (see Table S1) overnight at 4°C. Then slides were washed and incubated with Alexa Fluor 488- or 594-conjugated secondary antibody (712-545-150 and 611-585-215, Jackson ImmunoResearch Laboratories) for 1 h. Slides were mounted with DAPI (Molecular Probes) and then imaged using a Zeiss LSM710 confocal microscope.

For immunohistochemical analyses, the above primary antibody procedure was followed by incubation with biotin-labeled secondary antibodies (65-6140, Invitrogen) then Vectastain ABC kit and 3,3′-diaminobenzidine peroxidase substrate kit (Vector Laboratories) were used for color development. Slides were then counterstained with Hematoxylin and mounted.

Western blotting

Spermatogenic cells (5×10^4) were lysed in 2-mercaptoethanol-containing loading buffer and heated at 95°C for 5 min. SDS-PAGE and immunoblots were performed following standard procedures using a Mini-PROTEAN Tetra Cell System (Bio-Rad). The antibodies used are listed in Table S1.

Meiotic nuclear spreading and immunofluorescence staining

Testes were collected from adult male mice, and female ovaries were obtained from embryonic mice at E17.5-E18.5. Spreads were made as previously reported (Dia et al., 2017). Seminiferous tubules or embryonic ovaries were treated with hypotonic buffer [30 mM Tris, 5 mM EDTA, 50 mM sucrose, 17 mM trisodium citrate dehydrate and 0.5 mM dithiothreitol (pH 8.2)] a maximum of 30 min and then smashed in 100 mM sucrose buffer (pH 8.2). The suspension was then gently spread onto slides containing fixative buffer [1% PFA and 0.15% Triton X-100 (pH 9.2)]. After 2 h incubation in a humidity box, the slides were air-dried and washed in PBS three times before immunofluorescence staining. To stain, the slides were blocked with 10% donkey serum and incubated with primary antibody (see Table S1) for 1 h at room temperature. Then slides were washed and incubated with Alexa Fluor 488- or 594-conjugated secondary antibody (712-545-150 and 611-585-215, Jackson ImmunoResearch Laboratories), mounted, and imaged using a Zeiss LSM710 confocal microscope. Semiquantitative analysis of the fluorescence signals was conducted with the NIH Image program ImageJ.

MI chromosome spreads

We made a small improvement to the previously reported method (Evans et al., 1964). A suspension made in isotonic (2.2%) sodium citrate solution of a whole testis was centrifuged (500 ***g*** for 8 min) and resuspended in 1% sodium citrate solution for 12 min, sedimented again and fixed in a 3:1 mixture of absolute ethyl alcohol:glacial acetic acid. This was followed by two brief rinses in fresh fixative. Air-dried preparations were made from the final fixed suspension and stained with Giemsa.

Fluorescence *in situ* hybridization

We made probes following a previously reported method (Kauppi et al., 2011). Plasmid DNA (Chromosome Y: pY353/B; Chromosome X: DXWas70) was labeled with SpectumRed dUTP (Vysis, 30-803400) or

Development (2020) 147, dev183764. doi:10.1242/dev.183764

SpectrumGreen dUTP (Vysis, 30-803200), respectively, using a bioprime DNA labeling system (Invitrogen, 18094-011). FACS-isolated diploid cells were fixed on slides and then washed with 2×SSC (sodium saline citrate buffer) for 10 min at room temperature followed by a dehydration series of 80%, 90% and 100% ethanol for 2 min each. FISH probes described above were denatured on slides on a hot plate at 80°C for 8 min and hybridized at 37°C for 48 h. After washing, the slides were mounted with mounting media containing DAPI for DNA staining.

RNA-seq library preparation

Spermatocytes at different stages were collected from the indicated genotypes (500 cells per sample) using FACS as described above. Each sample was directly lysed with 4 µl lysis buffer (0.2% Triton X-100, RNase inhibitor, dNTPs, oligo-dT primers) and immediately used for cDNA synthesis using the Smart-seq2 method as described previously (Picelli et al., 2014). Sequencing libraries were constructed from 500 pg of amplified cDNA using TruePrep DNA Library Prep Kit V2 for Illumina (Vazyme, TD503) according to the manufacturer's instructions. Barcoded libraries were pooled and sequenced on the Illumina HiSeq X Ten platform to generate 150 bp paired-end reads.

ChIP-seq

Spermatocytes at different stages were isolated using FACS. H3K4me3 ChIP-seq libraries were generated from ∼10,000 spermatocytes using the ULI-NChIP-seq protocol as described previously (Brind'Amour et al., 2015). Briefly, spermatocytes were lysed with nuclear isolation buffer (Sigma-Aldrich), followed by MNase (NEB) digestion at 21°C for 7.5 min. The digested chromatin was then diluted in complete immunoprecipitation buffer, pre-cleared with 10 µl of protein A:protein G 1:1 Dynabeads (Thermo Fisher) and incubated with 58 ng of anti-H3K4me3 (Cell Signaling Technology, 9727, Lot6) and 10 µl of protein A:protein G 1:1 Dynabeads (Thermo Fisher) at 4°C overnight. ChIPed DNA was eluted in 100 mM $NaHCO_3$ and 1% SDS at 65°C for 1.5 h. Eluted DNA was then extracted using phenol:chloroform: isoamylol (25:24:1) and precipitated in 75% ethanol. The sequence libraries were generated using the NEBNext Ultra II DNA Library Prep Kit (NEB, E7645S) according to the manufacturer's instructions. Barcoded libraries were pooled and sequenced on the Illumina HiSeq X Ten platform to generate 150 bp paired-end reads.

RNA-seq data analysis

RNA-seq was performed with two biological replicates for all samples. Raw reads were trimmed to 50 bp and mapped to the mouse genome (mm9) with TopHat (v2.1.1) with default parameters. Uniquely mapped reads were subsequently assembled into transcripts guided by reference annotation [University of California at Santa Cruz (UCSC) gene models] with Cufflinks (v2.2.1). The expression level of each gene was quantified as FPKM, and FPKM values of replicates were averaged. Only expressed genes (FPKM>1 in at least one sample) were considered in all analyses. Functional annotation was performed with Metascape (http://metascape.org). Statistical analyses were implemented with R (http://www.rproject.org). The Spearman correlation coefficient (rs) was calculated using the 'cor' function, and the complete linkage hierarchical algorithm was used to cluster the genes. Quality information for the RNA-seq data used in this study is summarized in Table S2.

ChIP-seq data analysis

ChIP-seq reads were trimmed to 50 bp and aligned to the mouse genome build mm9 using bowtie2 (v2.3.4.1) with default parameters. All unmapped reads, non-uniquely mapped reads and PCR duplicates were removed. H3K4me3 peaks were called using MACS2 (v2.1.1.20160309) with the parameters -q 0.05 –nomodel –nolambda –broad –extsize 300 -B –SPMR -g mm and signal tracks for each sample were generated with the wig To BigWig tool from UCSC. The correlation between biological replicates and heat maps were generated using deeptools (v2.5.4). Biological replicates were analyzed together for each stage and for downstream analysis. Promoters were defined as 2 kb up- and downstream of annotated TSSs. The H3K4me3 intensity of different genomic regions was calculated using bedtools (v2.26.0) coverage command and normalized to FPKM. Quality information for the ChIP-seq data used in this study are summarized in Table S1.

Statistical analysis

Results are presented as mean±s.e.m. Most experiments included at least three independent samples and were repeated at least three times. The results for two experimental groups were compared using two-tailed unpaired Student's *t*-tests (*P<0.05, **P<0.01, ***P<0.001; n.s., not significant).

Competing interests

The authors declare no competing or financial interests.

Author contributions

Conceptualization: C.Y., Q.-Q.S., M.-H.T., H.-Y.F.; Methodology: M.-H.T., L.S.; Software: Y.-Z.Z.; Formal analysis: Y.-Z.Z., L.S.; Investigation: Y.J., H.-Y.Z., Z.L., C.Y.; Resources: M.-H.T.; Data curation: L.S.; Writing - original draft: Y.J., H.-Y.F.; Writing - review & editing: H.-Y.F.; Supervision: M.-H.T., L.S., H.-Y.F.; Project administration: Q.-Q.S., H.-Y.F.; Funding acquisition: H.-Y.F.

Funding

National Natural Science Foundation of China [31528016, 31871478, 31371449, 31671558]; National Key Research and Developmental Program of China [2016YFC1000600, 2017YFC1001500]; Natural Science Foundation of Zhejiang Province [LR18C060001]; Primary Research and Development Plan of Zhejiang Province [2017C03022]; Cao Guangbiao High Science and Technology Foundation, Zhejiang University.

Data availability

RNA-seq and ChIP-seq data have been deposited in the NCBI Gene Expression Omnibus database under accession number GSE133636. See http://genome.ucsc.edu/s/yezhang_zhu/Spermatocyte%2DCxxc1%2DRNA%2Dseq for the UCSC genome browser session for RNA-seq data. See http://genome.ucsc.edu/s/yezhang_zhu/Spermatocyte%2DCxxc1%2DChIP%2Dseq for the UCSC genome browser session for ChIP-seq data.

Supplementary information

Supplementary information available online at
http://dev.biologists.org/lookup/doi/10.1242/dev.183764.supplemental

Peer review history

The peer review history is available online at
https://dev.biologists.org/lookup/doi/10.1242/dev.183764.reviewer-comments.pdf

References

Adam, C., Guérois, R., Citarella, A., Verardi, L., Adolphe, F., Béneut, C., Sommermeyer, V., Ramus, C., Govin, J., Couté, Y. et al. (2018). The PHD finger protein Spp1 has distinct functions in the Set1 and the meiotic DSB formation complexes. *PLoS Genet.* **14**, e1007223. doi:10.1371/journal.pgen.1007223

Barlow, A. L., Benson, F. E., West, S. C. and Hultén, M. A. (1997). Distribution of the Rad51 recombinase in human and mouse spermatocytes. *EMBO J.* **16**, 5207-5215. doi:10.1093/emboj/16.17.5207

Baudat, F., Buard, J., Grey, C., Fledel-Alon, A., Ober, C., Przeworski, M., Coop, G. and de Massy, B. (2010). PRDM9 is a major determinant of meiotic recombination hotspots in humans and mice. *Science* **327**, 836-840. doi:10.1126/science.1183439

Berg, I. L., Neumann, R., Lam, K.-W. G., Sarbajna, S., Odenthal-Hesse, L., May, C. A. and Jeffreys, A. J. (2010). PRDM9 variation strongly influences recombination hot-spot activity and meiotic instability in humans. *Nat. Genet.* **42**, 859. doi:10.1038/ng.658

Borde, V., Robine, N., Lin, W., Bonfils, S., Géli, V. and Nicolas, A. (2009). Histone H3 lysine 4 trimethylation marks meiotic recombination initiation sites. *EMBO J.* **28**, 99-111. doi:10.1038/emboj.2008.257

Brind'Amour, J., Liu, S., Hudson, M., Chen, C., Karimi, M. M. and Lorincz, M. C. (2015). An ultra-low-input native ChIP-seq protocol for genome-wide profiling of rare cell populations. *Nat. Commun.* **6**, 6033. doi:10.1038/ncomms7033

Butler, J. S., Palam, L. R., Tate, C. M., Sanford, J. R., Wek, R. C. and Skalnik, D. G. (2009). DNA methyltransferase protein synthesis is reduced in CXXC finger protein 1-deficient embryonic stem cells. *DNA Cell Biol.* **28**, 223-231. doi:10.1089/dna.2009.0854

Cao, W., Guo, J., Wen, X., Miao, L., Lin, F., Xu, G., Ma, R., Yin, S., Hui, Z., Chen, T. et al. (2016). CXXC finger protein 1 is critical for T-cell intrathymic development through regulating H3K4 trimethylation. *Nat. Commun.* **7**, 11687. doi:10.1038/ncomms11687

Carlone, D. L. and Skalnik, D. G. (2001). CpG binding protein is crucial for early embryonic development. *Mol. Cell. Biol.* **21**, 7601-7606. doi:10.1128/MCB.21.22.7601-7606.2001

Chen, Y., Zheng, Y., Gao, Y., Lin, Z., Yang, S., Wang, T., Wang, Q., Xie, N., Hua, R., Liu, M. et al. (2018). Single-cell RNA-seq uncovers dynamic processes and critical regulators in mouse spermatogenesis. *Cell Res.* **28**, 879-896. doi:10.1038/s41422-018-0074-y

Chun, K. T., Li, B., Dobrota, E., Tate, C., Lee, J.-H., Khan, S., Haneline, L., HogenEsch, H. and Skalnik, D. G. (2014). The epigenetic regulator CXXC finger protein 1 is essential for murine hematopoiesis. *PLoS ONE* **9**, e113745. doi:10.1371/journal.pone.0113745

Cole, F., Keeney, S. and Jasin, M. (2012). Preaching about the converted: how meiotic gene conversion influences genomic diversity. *Ann. N. Y. Acad. Sci.* **1267**, 95-102. doi:10.1111/j.1749-6632.2012.06595.x

de Massy, B. (2013a). Initiation of meiotic recombination: how and where? Conservation and specificities among eukaryotes. *Annu. Rev. Genet.* **47**, 563-599. doi:10.1146/annurev-genet-110711-155423

de Massy, B. (2013b). Spp1 links sites of meiotic DNA double-strand breaks to chromosome axes. *Mol. Cell* **49**, 3-5. doi:10.1016/j.molcel.2012.12.011

Dia, F., Strange, T., Liang, J., Hamilton, J. and Berkowitz, K. M. (2017). Preparation of meiotic chromosome spreads from mouse spermatocytes. *J. Vis. Exp.*, **129**, e55378. doi:10.3791/55378

Diagouraga, B., Clément, J. A. J., Duret, L., Kadlec, J., de Massy, B. and Baudat, F. (2018). PRDM9 methyltransferase activity is essential for meiotic DNA double-strand break formation at its binding sites. *Mol. Cell* **69**, 853-865.e6. doi:10.1016/j.molcel.2018.01.033

Evans, E. P., Breckon, G. and Ford, C. E. (1964). An air-drying method for meiotic preparations from mammalian testes. *Cytogenet. Genome Res.* **3**, 289-294. doi:10.1159/000129818

Grey, C., Clément, J. A. J., Buard, J., Leblanc, B., Gut, I., Gut, M., Duret, L. and de Massy, B. (2017). In vivo binding of PRDM9 reveals interactions with noncanonical genomic sites. *Genome Res.* **27**, 580-590. doi:10.1101/gr.217240.116

Hinch, A. G., Zhang, G., Becker, P. W., Moralli, D., Hinch, R., Davies, B., Bowden, R. and Donnelly, P. (2019). Factors influencing meiotic recombination revealed by whole-genome sequencing of single sperm. *Science* **363**, eaau8861. doi:10.1126/science.aau8861

Holloway, J. K., Booth, J., Edelmann, W., McGowan, C. H. and Cohen, P. E. (2008). MUS81 generates a subset of MLH1-MLH3-independent crossovers in mammalian meiosis. *PLoS Genet.* **4**, e1000186. doi:10.1371/journal.pgen.1000186

Hunter, N. (2015). Meiotic recombination: the essence of heredity. *Cold Spring Harbor Perspect. Biol.* **7**, a016618. doi:10.1101/cshperspect.a016618

Imai, Y., Baudat, F., Taillepierre, M., Stanzione, M., Toth, A. and de Massy, B. (2017). The PRDM9 KRAB domain is required for meiosis and involved in protein interactions. *Chromosoma* **126**, 681-695. doi:10.1007/s00412-017-0631-z

Jones, G. H. (1984). The control of chiasma distribution. *Symp. Soc. Exp. Biol.* **38**, 293-320.

Kauppi, L., Barchi, M., Baudat, F., Romanienko, P. J., Keeney, S. and Jasin, M. (2011). Distinct properties of the XY pseudoautosomal region crucial for male meiosis. *Science* **331**, 916-920. doi:10.1126/science.1195774

Lin, Z., Hsu, P. J., Xing, X., Fang, J., Lu, Z., Zou, Q., Zhang, K.-J., Zhang, X., Zhou, Y., Zhang, T. et al. (2017). Mettl3-/Mettl14-mediated mRNA N(6)-methyladenosine modulates murine spermatogenesis. *Cell Res.* **27**, 1216-1230. doi:10.1038/cr.2017.117

Mahadevan, J. and Skalnik, D. G. (2016). Efficient differentiation of murine embryonic stem cells requires the binding of CXXC finger protein 1 to DNA or methylated histone H3-Lys4. *Gene* **594**, 1-9. doi:10.1016/j.gene.2016.08.048

Mézard, C., Jahns, M. T. and Grelon, M. (2015). Where to cross? New insights into the location of meiotic crossovers. *Trends Genet.* **31**, 393-401. doi:10.1016/j.tig.2015.03.008

Paigen, K. and Petkov, P. (2010). Mammalian recombination hot spots: properties, control and evolution. *Nat. Rev. Genet.* **11**, 221-233. doi:10.1038/nrg2712

Parvanov, E. D., Petkov, P. M. and Paigen, K. (2010). Prdm9 controls activation of mammalian recombination hotspots. *Science* **327**, 835-835. doi:10.1126/science.1181495

Parvanov, E. D., Tian, H., Billings, T., Saxl, R. L., Spruce, C., Aithal, R., Krejci, L., Paigen, K. and Petkov, P. M. (2017). PRDM9 interactions with other proteins provide a link between recombination hotspots and the chromosomal axis in meiosis. *Mol. Biol. Cell* **28**, 488-499. doi:10.1091/mbc.e16-09-0686

Picelli, S., Faridani, O. R., Björklund, A. K., Winberg, G., Sagasser, S. and Sandberg, R. (2014). Full-length RNA-seq from single cells using Smart-seq2. *Nat. Protoc.* **9**, 171-181. doi:10.1038/nprot.2014.006

Pittman, D. L., Cobb, J., Schimenti, K. J., Wilson, L. A., Cooper, D. M., Brignull, E., Handel, M. A. and Schimenti, J. C. (1998). Meiotic prophase arrest with failure of chromosome synapsis in mice deficient for Dmc1, a germline-specific RecA homolog. *Mol. Cell* **1**, 697-705. doi:10.1016/S1097-2765(00)80069-6

Sadate-Ngatchou, P. I., Payne, C. J., Dearth, A. T. and Braun, R. E. (2008). Cre recombinase activity specific to postnatal, premeiotic male germ cells in transgenic mice. *Genesis* **46**, 738-742. doi:10.1002/dvg.20437

Sha, Q.-Q., Dai, X.-X., Jiang, J.-C., Yu, C., Jiang, Y., Liu, J., Ou, X.-H., Zhang, S.-Y. and Fan, H.-Y. (2018). CFP1 coordinates histone H3 lysine-4 trimethylation and meiotic cell cycle progression in mouse oocytes. *Nat. Commun.* **9**, 3477. doi:10.1038/s41467-018-05930-x

Sherman, S. L., Petersen, M. B., Freeman, S. B., Hersey, J., Pettay, D., Taft, L., Frantzen, M., Mikkelsen, M. and Hassold, T. J. (1994). Non-disjunction of chromosome 21 in maternal meiosis I: evidence for a maternal age-dependent mechanism involving reduced recombination. *Hum. Mol. Genet.* **3**, 1529-1535. doi:10.1093/hmg/3.9.1529

Sollier, J., Lin, W., Soustelle, C., Suhre, K., Nicolas, A., Géli, V. and de La Roche Saint-André, C. (2004). Set1 is required for meiotic S-phase onset, double-strand break formation and middle gene expression. *EMBO J.* **23**, 1957-1967. doi:10.1038/sj.emboj.7600204

Sommermeyer, V., Béneut, C., Chaplais, E., Serrentino, M. E. and Borde, V. (2013). Spp1, a member of the Set1 Complex, promotes meiotic DSB formation in promoters by tethering histone H3K4 methylation sites to chromosome axes. *Mol. Cell* **49**, 43-54. doi:10.1016/j.molcel.2012.11.008

Stanzione, M., Baumann, M., Papanikos, F., Dereli, I., Lange, J., Ramlal, A., Tränkner, D., Shibuya, H., de Massy, B., Watanabe, Y. et al. (2016). Meiotic DNA break formation requires the unsynapsed chromosome axis-binding protein IHO1 (CCDC36) in mice. *Nat. Cell Biol.* **18**, 1208-1220. doi:10.1038/ncb3417

Thomson, J. P., Skene, P. J., Selfridge, J., Clouaire, T., Guy, J., Webb, S., Kerr, A. R. W., Deaton, A., Andrews, R., James, K. D. et al. (2010). CpG islands influence chromatin structure via the CpG-binding protein Cfp1. *Nature* **464**, 1082. doi:10.1038/nature08924

Tian, H., Billings, T. and Petkov, P. M. (2018). CXXC1 is not essential for normal DNA double-strand break formation and meiotic recombination in mouse. *PLoS Genet.* **14**, e1007657. doi:10.1371/journal.pgen.1007657

Vincenten, N., Kuhl, L.-M., Lam, I., Oke, A., Kerr, A. R. W., Hochwagen, A., Fung, J., Keeney, S., Vader, G. and Marston, A. L. (2015). The kinetochore prevents centromere-proximal crossover recombination during meiosis. *eLife* **4**, e10850. doi:10.7554/eLife.10850

Wang, X., Kang, J.-Y., Wei, L., Yang, X., Sun, H., Yang, S., Lu, L., Yan, M., Bai, M., Chen, Y. et al. (2019). PHF7 is a novel histone H2A E3 ligase prior to histone-to-protamine exchange during spermiogenesis. *Development* **146**, dev175547. doi:10.1242/dev.175547

Yu, C., Fan, X., Sha, Q.-Q., Wang, H.-H., Li, B.-T., Dai, X.-X., Shen, L., Liu, J., Wang, L., Liu, K. et al. (2017). CFP1 regulates histone H3K4 trimethylation and developmental potential in mouse oocytes. *Cell Rep.* **20**, 1161-1172. doi:10.1016/j.celrep.2017.07.011

Figure S1

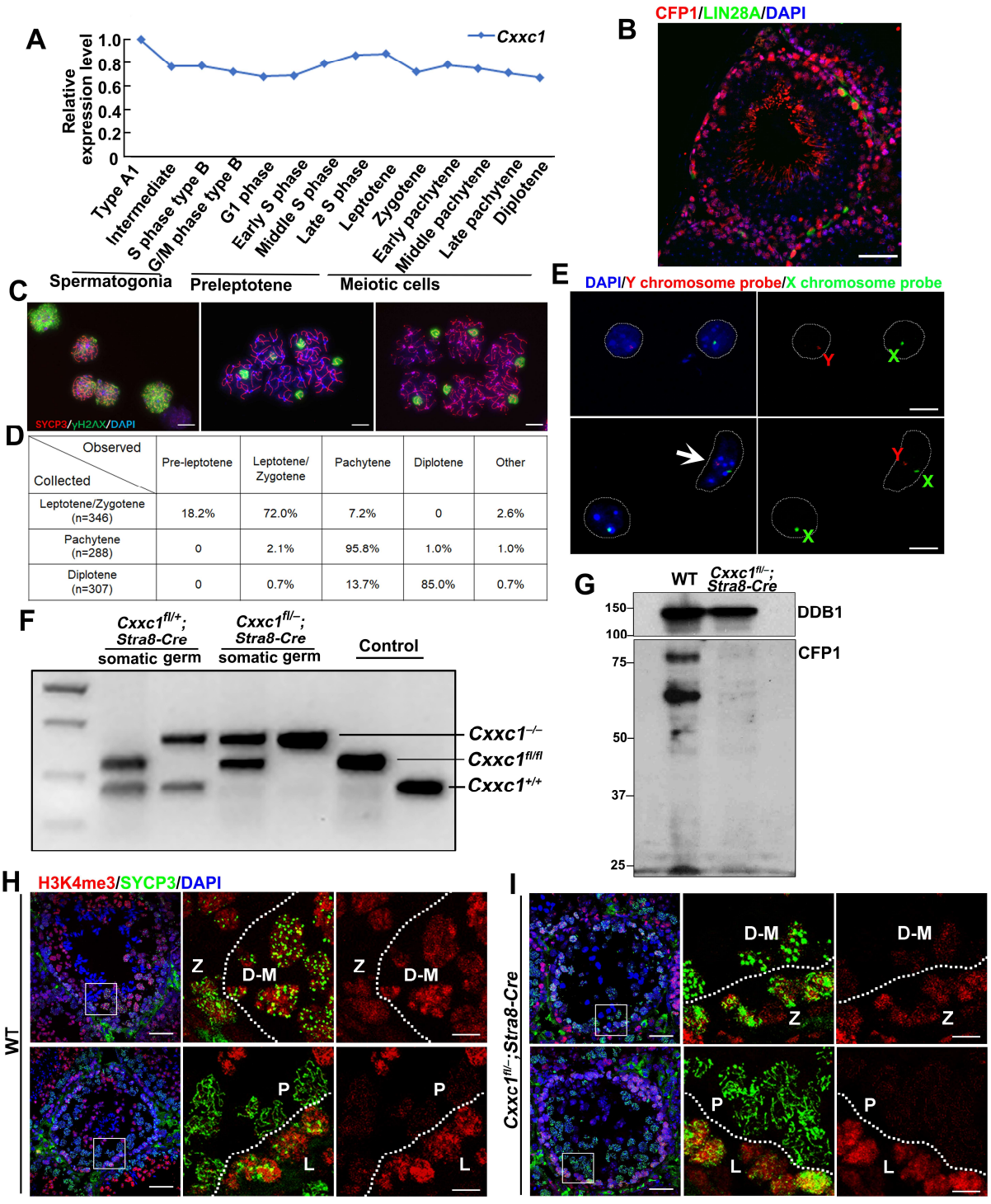

Figure S1. CFP1 is indispensable for H3K4me3 maintenance during spermatogenesis.

A: Relative expression level of *Cxxc1* from spermatogonia to meiotic cells from published single-cell RNA-seq dataset (Chen et al., 2018). **B:** Immunofluorescent co-staining of LIN28A and CFP1 in testes of 12-week-old WT mice. DNA was counterstained with DAPI. Scale bar = 50 μM. **C:** Representative images showed the sorted Leptotene/Zygotene (L/Z), Pachytene (P) and Diplotene (D) spermatocytes. The spread nuclei were double labeled with γH2AX (green) and SYCP3 (red) and co-stained with DAPI (blue). Scale bars = 20 μm. **D:** Percent purity quantification based on immunofluorescence analysis after cell sorting. Cell purity was calculated as (cell type observed/total cells) × 100%. **E:** Representative images of FISH assay of X and Y chromosome on FACS-isolated diploid cells. The white arrow indicated a somatic cell with both X and Y chromosome and the others were secondary spermatocytes with either X or Y chromosome. Scale bars = 20 μm. **F:** Genotyping of somatic cells and Cre-mediated recombined germ cells in heterozygous and knockout mice. **G:** Western blot using an antibody targeting CFP1 N-terminal region in spermatogenic cells isolated from adult WT and *Cxxc1*$^{fl/-}$*;Stra8-Cre* mice. **H and I:** Left tri-color panel, Immunofluorescent co-staining of SYCP3 and H3K4me3 in testes of 12-week-old WT and *Cxxc1*$^{fl/-}$*;Stra8-Cre* mice. DNA was counterstained with DAPI. Scale bar = 50 μM. Right two panels are enlarged images. Scale bar = 200 μM.

Figure S2

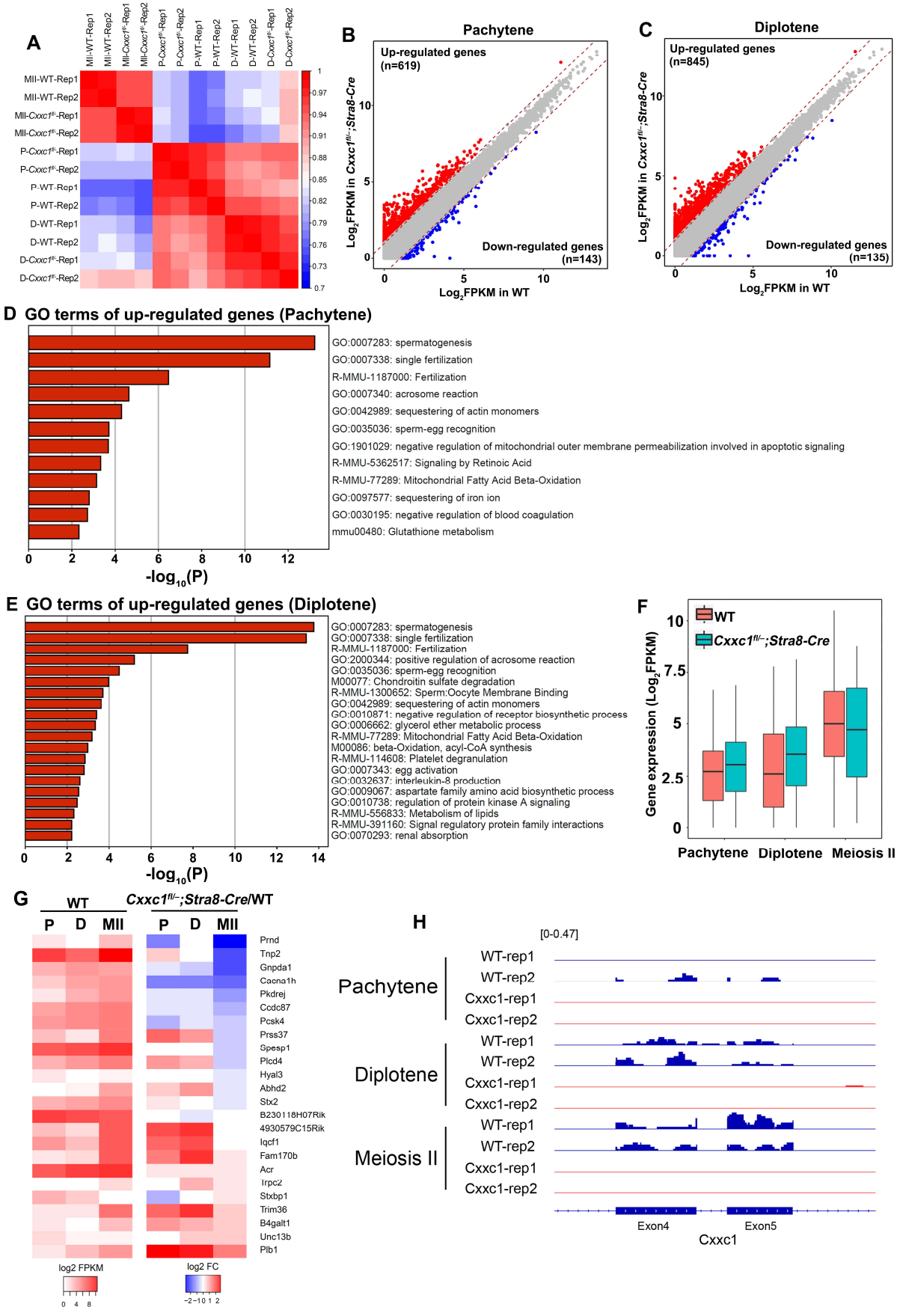

Figure S2. RNA-seq analyses of pachytene, diplotene and MII spermatocytes derived from WT, *Cxxc1* cKO mice

A: Heatmap of spearman correlation coefficients of total transcripts among WT and *Cxxc1*-null spermatocytes at different stages. **B and C:** Scatter plot comparing transcripts between WT and *Cxxc1* cKO spermatocytes at pachytene (B) and diplotene (C) stages. Genes up-regulated (FC>2.0) and down-regulated (FC<2.0) in *Cxxc1* cKO spermatocytes are colored with red and blue, respectively. **D and E:** Gene ontology analysis of up-regulated genes in *Cxxc1*-null spermatocytes at pachytene (D) and diplotene (E) stages. **F and G:** Box plot and heatmap showing varying gene expressive level of acrosome-reaction genes (GO: 0007340) among WT and *Cxxc1*-null spermatocytes at different stages. **H:** Snapshot of RNA-seq data showing the deletion of *Cxxc1* exons.

Figure S3

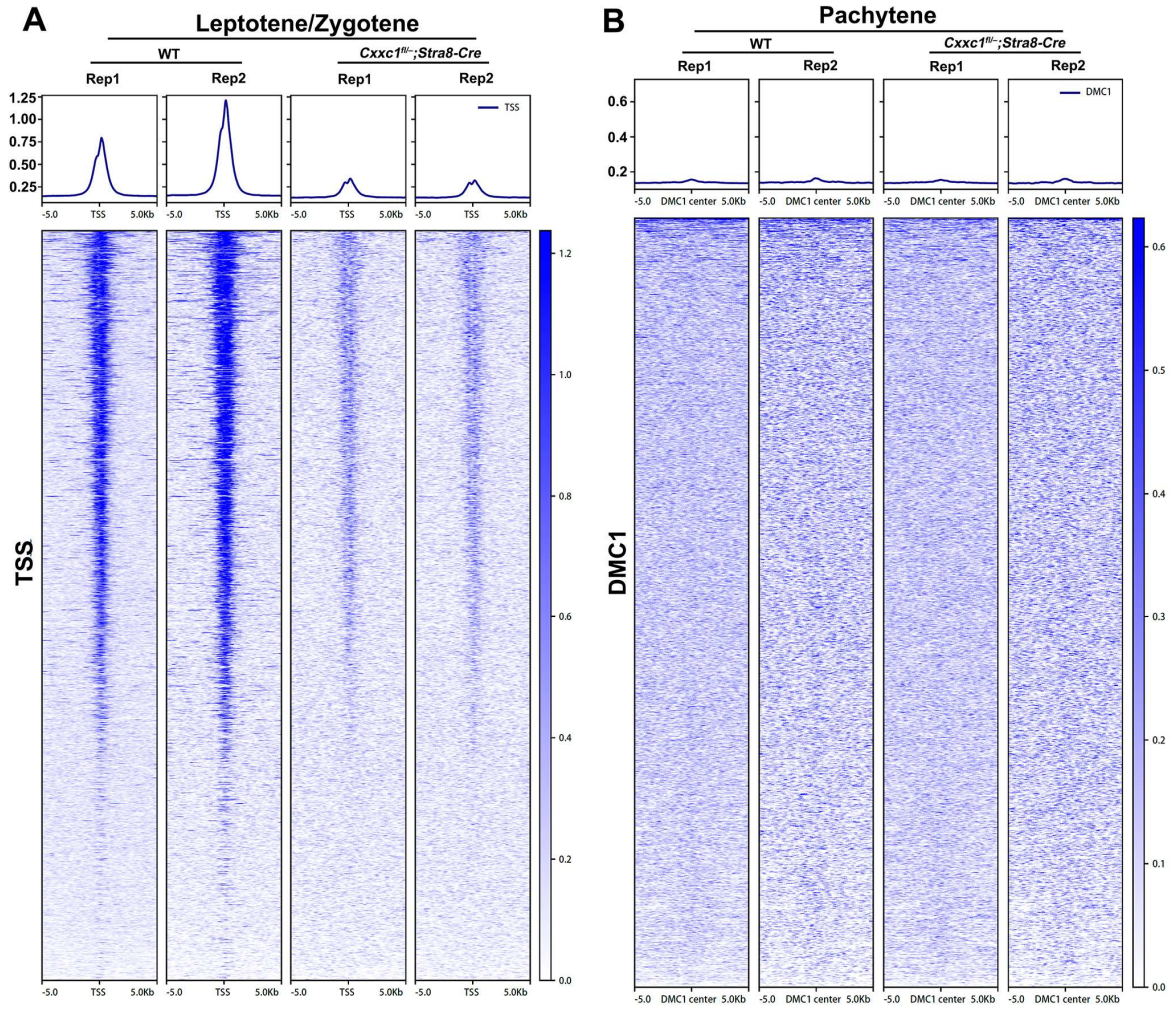

Figure S3. H3K4me3 ChIP-seq analyses of leptotene/zygotene and pachytene spermatocytes derived from WT, *Cxxc1* cKO mice

A: Heatmap of H3K4me3 levels in WT and *Cxxc1*-null leptotene/zygotene spermatocytes at the TSS regions. **B:** Heatmap of H3K4me3 levels in WT and *Cxxc1*-null pachytene spermatocytes at the centers of DMC1-binding sites.

Table S1. Antibody information

Protein name	Manufacture (catalogue number)	Applications (working dilution)	Website Link
H3K4me1	Cell Signaling (5326)	WB (1:1000)	http://www.cst-c.com.cn/products/primary-antibodies/mono-methyl-histone-h3-lys4-d1a9-xp-rabbit-ab/5326?_=1508331672321&Ntt=&tahead=true
H3K4me2	Cell Signaling (9725)	WB (1:1000)	http://www.cst-c.com.cn/products/primary-antibodies/di-methyl-histone-h3-lys4-c64g9-rabbit-mab/9725?_=1508331697704&Ntt=H3K4me&tahead=true
H3K4me3	Abcam (ab8580)	IF (1:400) WB (1:1000)	http://www.abcam.com/histone-h3-tri-methyl-k4-antibody-chip-grade-ab8580.html
α-Tubulin	Sigma (F2168)	WB (1:1000)	http://www.sigmaaldrich.com/catalog/product/sigma/f2168?lang=zh&region=CN
CFP1	Abcam (ab198977)	WB (1:500); IF (1:100) IHC(1:100)	http://www.abcam.com/cgbp-antibody-epr19199-ab198977.html
CFP1-N terminus	Abcam (ab189829)	WB (1:1000)	https://www.abcam.com/CGBP-antibody-N-terminal-ab189829.html?utm_source=labome&utm_medium=paid_referral&utm_term=1RY_CGBP_ab189829
SYCP3	Homemade	IF (1:400)	Immunogen: Full length of mouse SYCP3
SYCP1	Abcam (ab15087)	IF (1:200)	https://www.citeab.com/antibodies/771942-ab15087-anti-scp1-antibody
H2AK119ub1	Cell Signaling (8240)	WB (1:2000)	https://www.cst-c.com.cn/products/primary-antibodies/ubiquityl-histone-h2a-lys119-d27c4-xp-rabbit-mab/8240?site-search-type=Products
H3K27me3	Abcam (ab9733)	WB (1:1000)	https://www.cst-c.com.cn/products/primary-antibodies/tri-methyl-histone-h3-lys27-c36b11-rabbit-mab/9733?site-search-type=Products
MVH	Abcam (ab13840)	IF (1: 200); IHC (1: 400)	http://www.abcam.com/ddx4--mvhantibody-ab13840.html

γH2AX	Cell Signaling (9718S)	IF (1: 400)	https://www.cellsignal.com/products/primary-antibodies/phospho-histone-h2a-xser139-20e3-rabbitmab/9718?N=4294956287&Ntt=h2a.x&fromPage=plp
MLH1	Proteintech (11697-1-AP)	IF (1: 100)	https://www.ptglab.com/products/MLH1-Antibody-11697-1-AP.htm
CREST	Fitzgerald Industries International (70R-21494)	IF (1:100)	https://www.fitzgerald-fii.com/crest-antibody-70r-21494.html
DMC1	Proteintech (13714-1-AP)	IF (1: 100)	https://www.ptglab.com/Products/DMC1-Antibody-13714-1-AP.htm
Rad51	Abcam (ab176458)	IF (1: 100)	http://www.abcam.com/rpa70-antibodyab87272.html
PNA	Sigma (L7381)	IF (1: 500)	https://www.sigmaaldrich.com/catalog/product/sigma/l7381?lang=zh&region=CN
Lin28a	R&D Systems	IF (1: 200)	https://www.rndsystems.com/cn/products/human-lin-28a-antibody_af3757

Table S2. Summary of sequencing information

Type	Sample	Total reads	Mapping efficiency	Uniquely mapping efficiency	Correlation
RNA-seq	P-WT-Rep1	16,984,226	88.41%	78.72%	0.965
	P-WT-Rep2	20,610,839	88.12%	81.88%	
	P-*Cxxc1*$^{fl/-}$-Rep1	16,179,726	90.22%	82.18%	0.980
	P- *Cxxc1*$^{fl/-}$-Rep2	22,555,557	86.69%	78.11%	
	D-WT-Rep1	20,124,165	92.72%	86.80%	0.978
	D-WT-Rep2	21,454,127	89.78%	84.51%	
	D- *Cxxc1*$^{fl/-}$-Rep1	20,723,889	93.36%	87.26%	0.971
	D- *Cxxc1*$^{fl/-}$-Rep2	19,643,176	91.66%	85.87%	
	MII-WT-Rep1	19,902,160	91.86%	86.38%	0.980
	MII-WT-Rep2	20,810,855	90.34%	85.60%	
	MII- *Cxxc1*$^{fl/-}$-Rep1	19,101,599	92.93%	87.52%	0.978
	MII- *Cxxc1*$^{fl/-}$-Rep2	17,072,060	91.80%	85.57%	
ChIP-seq	L/Z-WT-Rep1	27,322,505	94.73%	67.77%	0.94
	L/Z-WT-Rep2	14,196,091	94.17%	69.14%	
	L/Z-*Cxxc1*$^{fl/-}$-Rep1	13,905,388	85.25%	61.81%	0.97
	L/Z- *Cxxc1*$^{fl/-}$-Rep2	14,497,563	93.52%	67.58%	
	P-WT-Rep1	26,641,654	96.38%	66.95%	0.91
	P-WT-Rep2	11,196,777	94.27%	67.16%	
	P- *Cxxc1*$^{fl/-}$-Rep1	24,615,804	96.32%	65.40%	0.89
	P- *Cxxc1*$^{fl/-}$-Rep2	11,252,776	91.04%	64.83%	